Estimation of NAPL-Water interfacial areas for unconsolidated porous media by kinetic interface sensitive (KIS) tracers

Alexandru Tatomir[1,2], Huhao Gao[2], Christopher Pötzl[3], Nikolaos Karadimitriou[4], Tobias Licha[5], Holger Class[6], Rainer Helmig[6], and Martin Sauter[2]

[1]Department of Earth Sciences, Geocentrum, Uppsala University, Villavägen 16, 752 36 Uppsala, Sweden.

[2]Department of Applied Geology, Geoscience Centre of the University of Göttingen, Goldschmidtstr. 3, 37077 Göttingen, Germany

[3]Department of Structural Geology and Geodynamics, Geoscience Centre of the University of Göttingen, Goldschmidtstr. 3, 37077 Göttingen, Germany

[4]Department of Structural Engineering, University of Stuttgart, Pfaffenwaldring 7, 70569 Stuttgart, Germany

[5]Department of Applied Geology, Institute of Geology, Mineralogy and Geophysics, Ruhr University Bochum, Universitätsstr. 150, 44801 Bochum, Germany

[6]Department of Hydromechanics and Modelling of Hydrosystems, University of Stuttgart, Pfaffenwaldring 7, 70569 Stuttgart, Germany

Corresponding author: Alexandru Tatomir (alexandru.tatomir@geo.uu.se; alexandru.tatomir@geo.uni-goettingen.de)

Key Words:

- Kinetic Interface Sensitive (KIS) tracers
- Fluid-fluid interfacial area
- Multiphase flow in porous media
- Reactive transport in porous media
- Immiscible displacement
- Column experiments
- Terminal menisci

Submitted to: *Water Resources Research*

Abstract

Employing kinetic interface sensitive (KIS) tracers, we investigate three different types of glass-bead materials and two natural porous media systems to quantitatively characterize the influence of the porous-medium grain-, pore-size and texture on the “mobile” interfacial area between an organic liquid and water. By interpreting the breakthrough curves (BTCs) of the reaction product of the KIS tracer hydrolysis we obtain a relationship for the specific interfacial area (IFA) and wetting saturation. The immiscible displacement process coupled with the reactive tracer transport across the fluid-fluid interface is simulated with a Darcy-scale numerical model. The results show that the current reactive transport model is not always capable to reproduce the breakthrough curves of tracer experiments and that a new theoretical framework is required.

Total solid surface area of the grains, i.e., grain surface roughness, is shown to have an important influence on the capillary-associated IFA by comparing results obtained from experiments with spherical glass beads having very small or even no surface roughness and those obtained from experiments with the natural sand. Furthermore, a linear relationship between the mobile capillary associated IFA and the inverse mean grain diameter can be established. The results are compared with the data collected from literature measured with high resolution microtomography and partitioning tracer methods. The capillary associated IFA values are consistently smaller because KIS tracers measure the mobile part of the interface. Through this study the applicability range of the KIS tracers is considerably expanded and the confidence in the robustness of the method is improved.

1 Introduction

The interfacial area between fluid-phases plays a critical role in the coupled multiphase flow, solute transport and reaction processes in porous media (Miller et al. 1990; Hassanizadeh and Gray 1990; Reeves and Celia 1996). Some applications, where the fluid-fluid interfacial area (FIFA) plays a major role, are the geological storage of CO_2 (e.g., Niemi et al. 2016), oil and gas recovery, the remediation of contaminated sites, such as per- and poly-fluoroalkyl substances (PFAS) (e.g., Brusseau 2018; Brusseau 2019).

The fluid-fluid interfacial areas can be classified in capillary-associated interfacial areas (IFAs) (e.g., menisci), and film-associated interfacial areas, or surface-adsorbed (Costanza-Robinson and Brusseau 2002; Brusseau et al. 2006; Porter et al. 2010). The sum of the two represents the total interfacial area. The capillary-associated IFA, a_{wn}, can be further subdivided into immobile (or stagnant), $a_{wn}^{immobile}$, or mobile, a_{wn}^{mobile} (Figure 1) (Joekar-Niasar and Hassanizadeh 2012a)

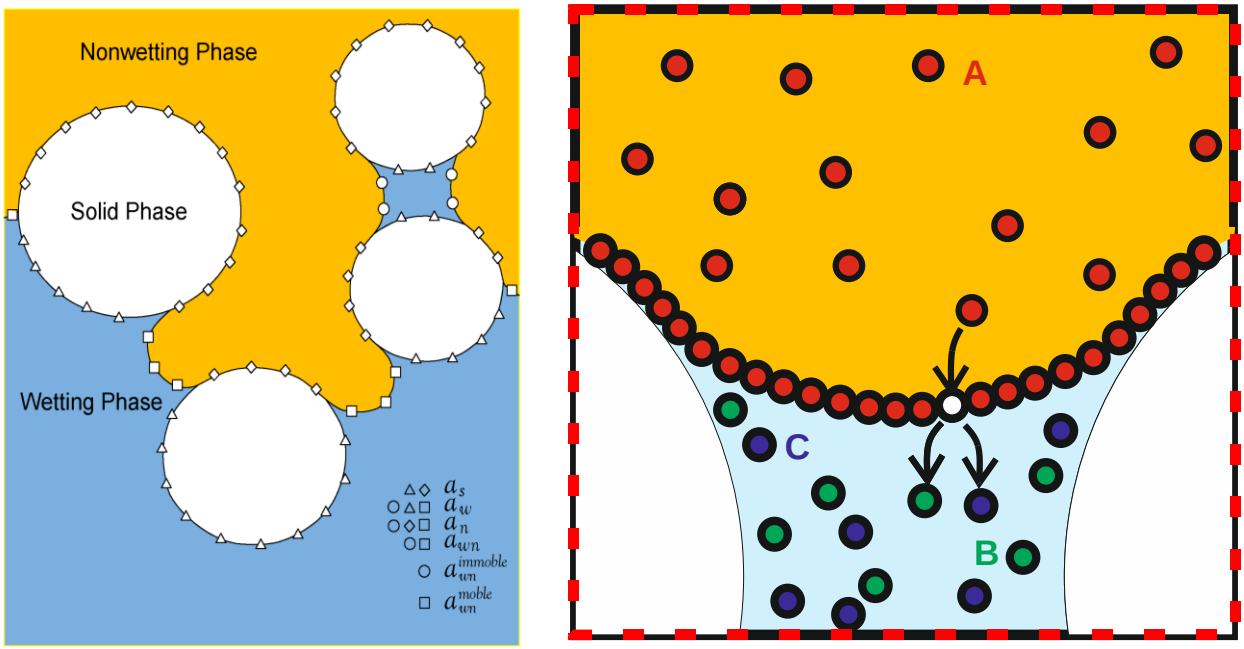

a) b)

Figure 1: a) Illustration of the different types of interfacial areas b) KIS tracer (A) adsorption on the fluid-fluid interface, followed by hydrolysis to form two by-products (B+C) dissolved in water, an acid and alcohol.

1.1 Models for calculating the FIFA

Due to difficulties in directly measuring the FIFA, initial studies focused on developing theoretical and modelling approaches employing normalized interfacial area per unit of representative elementary volume (REV) (Leverett 1941; Gvirtzman and Roberts 1991; Hassanizadeh and Gray 1993; Cary 1994; Reeves and Celia 1996; Bradford and Leij 1997; Held and Celia 2001; Oostrom et al. 2001; Dalla et al. 2002; Dobson et al. 2006) The models can be roughly classified into the following categories: pore-geometry models, where the porous media is represented using an idealized spherical packing (e.g., Gvirtzman and Roberts 1991; Likos and Jaafar 2013), or a bundle of capillary tubes (Cary 1994; Oostrom et al. 2001), and thermodynamic-based models (Leverett 1941; Bradford and Leij 1997; Grant and Gerhard 2007)

measuring the net amount of reversible work. With the development of computational capabilities other categories were added: pore-network models that use a simplified representation of the porous media as a network of pore-bodies and pore-throats (Reeves and Celia 1996); pore-morphology models (e.g., (Dalla et al. 2002); and direct pore-scale numerical simulations using particle-based methods such as the Lattice Boltzmann (Porter et al. 2010), and smooth particle hydrodynamics, and grid-based computational fluid dynamics methods such as the level-set-, volume-of-fluid-, and phase field-methods (Gao et al. 2020). The pore-scale models calculate explicitly the magnitude of FIFA and allow the calculation of upscaled per-volume normalized quantities, i.e., capillary pressure, saturation and specific interfacial areas, required by the continuum-based, Darcy-scale multiphase flow simulators. The expression of the FIFA as volume averaged quantity allows its straightforward implementation into the Darcy-scale type flow simulators since no additional parameters other than the initial ones are required.

1.2 Measurement techniques for fluid-fluid interfacial area

Several experimental methods were proposed to measure the fluid-fluid interfacial areas (FIFAs): interface partitioning tracer test (IPTT), where the tracer is dissolved in aqueous (Kim et al. 1997; Saripalli et al. 1997; Anwar et al. 2000; Brusseau et al. 2007) or in gaseous phase (Kim et al. 1999; Costanza-Robinson and Brusseau 2002), high-resolution industrial X-ray microtomography (XMT), and synchrotron XMT (Culligan et al. 2006; Brusseau et al. 2008; Narter and Brusseau 2010; Porter et al. 2010; Peche et al. 2016; McDonald et al. 2016; Lyu Ying et al. 2017; Patmonoaji et al. 2018; Araujo and Brusseau 2020), the gas adsorption chemical reaction (GACR) (Lyu Ying et al. 2017), thin micro-models (Karadimitriou et al. 2016), and the kinetic interface sensitive tracer method (Tatomir et al. 2018). The experimental methods for measuring the FIFA are usually applied in controlled laboratory conditions, i.e. tracer methods, XMT, micro models, (e.g., Dobson et al. 2006; Porter et al. 2010; Karadimitriou et al. 2016; McDonald et al. 2016; Tatomir et al. 2018), but also in the field, i.e. tracer methods (Nelson and Brusseau 1996; Annable et al. 1998; Simon and Brusseau 2007). Some methods are inherently designed for laboratory conditions only, e.g. micro-models, and XMT.

Usually, standard tracer techniques measure the FIFA in steady state conditions, when a residual saturation is formed. For instance, the gas-phase IPTT implies that a residual water saturation is created in the column, while the gas phase together with two tracers, a conservative and a reactive one, being circulated. The tracer partitioning on the fluid-fluid interface is interpreted from breakthrough curves (BTCs) and the FIFA is calculated.

Most of the literature related to measurement of FIFA address to air-water fluid systems. However, there is a consistent body of literatures which addresses to NAPL-water or organic fluid-water fluid systems (Dobson et al. 2006; Schnaar and Brusseau 2006; Brusseau et al. 2008; Brusseau et al. 2009; Narter and Brusseau 2010; Brusseau et al. 2010; Zhong et al. 2016; Tatomir et al. 2018).

The kinetic interface sensitive (KIS) tracer method was proposed by Tatomir et al. (2018) for quantifying the FIFA in a dynamic immiscible displacement process. A proof of concept was provided using controlled column experiments with a well-characterized glass-bead porous medium. The experimental results were interpreted by specifically developed numerical models for multiphase flow coupled with reactive transport showing a general agreement of the FIFA size with the theory. KIS tracers are first dissolved in the non-wetting phase and then injected. When they come in contact with water, they hydrolyze to form two highly soluble components in water, i.e., an acid and an alcohol. A KIS tracer stable component, with a zero-order reaction rate

was synthesized by Schaffer et al. (2013). The interpretation of the breakthrough curves of the "byproduct acid" provides information about the size of the FIFA. Since the measurements are performed for the tracer arriving at the outlet together with the mobilized water, KIS tracers are considered to measure the mobile component of the capillary associated interface, a_{wn}^{mobile}.

1.3 Studies comparing the experimental methods for FIFA measurement

The magnitude of the FIFA reported in the literature depends on the measurement technique employed. This is because it is not always clear which part of the FIFA a particular technique measures, either the total interfacial area, the capillary-associated IFA, or some combination of both the capillary-associated IFA and some part of the film associated area.

Thus, compared to aqueous-phase IPTT the gas-phase IPTT generally yields larger IFA (Costanza-Robinson and Brusseau 2002). It is hypothesized that the gas-phase IPTT measures both capillary and film-adsorbed FIFA while the aqueous-phase IPTT measure primarily FIFA formed by water held by capillarity, e.g. pendular rings. At low water saturations the FIFA measured with gas-phase IPTT showed exponential increase (Kim et al. 1999; Costanza-Robinson and Brusseau 2002; Peng and Brusseau 2005). Similarly, using gas-phase IPTT, Peng and Brusseau (2005) showed that at low water saturations, the maximum air-water IFA approached those of the normalized solid surface areas, a_s. This indicates that indeed the gas phase IPTT measure the total FIFA, as this was orders of magnitude larger than the calculated, GSSA, but in good agreement with the SSSA measured with N_2/BET method.

Several studies reported that IPTT measured FIFAs were larger than those measured with XMT, which can only scan with a certain resolution (Brusseau et al. 2006; Brusseau et al. 2007; Brusseau et al. 2010; Brusseau et al. 2015; McDonald et al. 2016). Narter and Brusseau (2010) compared the aqueous-phase IPTT with high-resolution micro-tomography for an organic liquid-water -glass bead porous medium system, in an attempt to address the hypothesis that the surface roughness has an influence on the FIFA. Their findings suggest that IPTT and micro-tomography provide robust FIFA values that are comparable when the porous medium has no surface roughness. In that sense, the maximum specific FIFA, was similar to the SSSA measured with N_2/BET and using the smooth-sphere assumption. (Narter and Brusseau 2010; Zhong et al. 2016; Lyu Ying et al. 2017). An explanation for this is that the computed micro-tomography measured IFAs do not include areas associated with microscopic surface heterogeneities, i.e. roughness-associated surface area (Brusseau et al. 2009; Brusseau et al. 2010). A review of the tracer-based methods for measuring air-water IFAs is provided in (Costanza-Robinson and Brusseau 2002), while the various sources of error of the IPTT are discussed in (Brusseau et al. 2008).

Note that relationships between the capillary associated IFA and the size of the total interfacial area can be established. Grant and Gerhard (2007) used the previous pore-network data of Dalla et al. (2002) to obtain the ratio of capillary-associated IFA to total IFA as a function of the saturation. Thus, the total IFA obtained from their thermodynamic model is able to be related to capillary-associated IFA for a given fluid saturation.

1.4 Porous media characteristics influence on FIFA

The size of FIFA is mediated by the pore-scale fluid configuration effects which are hard to quantify. At the macro-scale, the FIFA is usually expressed as a function of fluid saturation. Also, the capillary-associated IFA was observed to increase monotonically with increasing capillary pressure and then to plateau at values that correspond to areas associated with residual water saturation (Brusseau et al. 2006)

Literature studies have shown that porous medium texture influences the FIFAs, namely, porous media with larger solid surface areas generate larger fluid-fluid interfacial areas. Several studies demonstrate that fluid-fluid interfacial area is a function of soil properties such as **grain size**, **grain size distribution**, and **surface roughness** (Cary 1994; Anwar et al. 2000; Peng and Brusseau 2005; Cho and Annable 2005; Dobson et al. 2006; Brusseau et al. 2008; Brusseau et al. 2009; Brusseau et al. 2010; Jiang et al. 2020)**.** In the following, the available studies of major relevance on the influence of these parameters are described.

1.4.1 Grain-size influence on fluid-fluid interfacial area

Both the IFA models and experiments show that the maximum total specific FIFA is a function of inverse median grain diameter (e.g., Anwar et al. 2000; Brusseau et al. 2009).Costanza and Brusseau (2000) used the theoretical model-based data reported by (Cary 1994) to evaluate the influence of porous-medium grain size on FIFA. One observation of these studies was that porous media with smaller grain sizes have larger specific FIFAs. Using four high purity sands (Dobson et al. 2006) conducted aqueous-phase interface-partitioning tracer tests in NAPL-water fluid systems and compared the results with the theoretical models (Bradford and Leij 1997; Oostrom et al. 2001) and a modified version of (Bradford and Leij 1997). Even though the measured specific IFA were increasing with decreasing median grain diameter, not all the reported experimental results (only three out of four) were following the theoretically expected trend.

Brusseau et al. (2009) use ten porous media to study the influence of grain-size and texture on FIFA. The results show that the specific FIFA and maximum specific FIFA correlate very well with the inverse grain diameter. Also, the IFA correlates with SSSA and with the inverse median grain diameter (IMGD). This, however, is obtained with tracer techniques which are indirect measurement of IFA (Brusseau et al. 2009).

1.4.2 Porous-medium-texture influence on the fluid-fluid interfacial area

Besides the mean grain diameter, surface roughness is one of key parameters influencing not only the fluid-fluid interface, but also the degree of wettability, the permeability of the medium, or the capillary pressure- and relative permeability-saturation relationships.

Peng and Brusseau (2005) used the gas phase IPTT to measure the air-water FIFA for eight soils and natural sands. The values were compared to the normalized surface areas of the porous media. It was observed that FIFAs were generally larger for materials with larger SSSA measured with N_2/BET method, incorporating the surface roughness.

Analyzing ten different types of porous media, comprising different grain-size distributions and geochemical properties, Brusseau et al. (2009) report that grain-size distributions have minimal impact on the FIFA. Brusseau et al. (2010) conducted aqueous phase IPTT on two soils (Vinton and Eustis) and found that the maximum NAPL -water IFAs are much larger than those obtained by geometric calculation with the smooth-sphere assumption (GSSA). Their observations suggest that surface roughness has a significant impact on interfacial area and that the glass beads' total specific IFA is similar to the SSSA predicted using the smooth-sphere assumption. A linear relationship between the total solid area measured with N_2/BET and the IPTT-measured IFA is established. However, this is based on a total of seven measurements, one very large N_2/BET value being dominant. Because the film-associated areas are a significant component of the FIFAs measured with IPTT, they conclude that the IPTT methods measure some fraction of the interfacial area associated with surface roughness.

Zhong et al. (2016) used a modified version of aqueous-phase IPTT to measure FIFA for several porous media made of glass beads, sand and Vinton soil during a series of drainage and

imbibition. The modified IPTT allows measuring the IFA at higher saturations than residual. The maximum total FIFAs were compared to the SSSA measured with N_2/BET and to those estimated based on GSSA.

Recently, Jiang et al. (2020) investigated the role of microscale surface roughness on the FIFA assuming a triangular bundle-of-cylindrical capillaries, their model belonging to the pore-geometry model category. The exponential increase of the total FIFA observed with the gas-phase IPTT method when wetting saturation approaches zero can be explained by the impact of surface roughness on the film-associated IFA.

1.5 Objective

To date, the KIS tracer method has been tested only for an ideal glass-bead well-sorted uniform medium. An important step in the development of the KIS tracer method is the implementation of the method for different soil types followed by the interpretation and comparison of the results. Two categories of porous media are to be used, glass-beads and natural sands, having different textures, grain- and pore-size distributions. By extending the applicability range of the KIS tracers to several porous media, the generated set of tracer breakthrough curves is used, subsequently, to verify the current modelling approaches.

For understanding the influence of **mean grain size**, **grain and pore-size distributions**, and **surface roughness,** on the IFA, an extensive characterization of the glass beads and of the natural sand is initially performed with digital image analysis and mercury intrusion porosimetry. Our objective is to compare the IFA, obtained by KIS-tracer experiments in terms of the maximum capillary associated specific interfacial area with published experimental data using various measurement techniques and models.

2 Materials and methods

2.1 Materials

2.1.1 Laboratory setup

The testing procedure and experimental apparatus are those of our previous study (Tatomir et al. 2018). The experimental apparatus (Figure 2) consists of a stainless-steel column, 250 mm long and 30 mm in diameter. Two metal frits with extremely fine meshes are placed either end of the column holding the sand inside the column. A peristaltic pump with adjustable flow rate is first used for saturating the column with water and later for providing a constant flow to the bottom of the vertically oriented column of n-octane with dissolved KIS tracer. The peristaltic pump can set the ratio of working power, but the actual flow rate depends on the permeability of the system.

The chemical stability of the materials (e.g., tubings, column) was tested in the presence of ultra-pure water and n-octane. We observed that many carbon-based materials (i.e., tubings) interact with the n-octane inducing either swelling or brittleness. Therefore, only materials which did not react with n-octane were selected when constructing the experimental setup **Figure 2**. Naphthalenesulfonates are highly fluorescent and can be detected at low concentration levels in the range of μg/l using fluorescence spectrometry. The 2-NSA concentration in water was measured using a Cary Eclipse fluorescence spectrophotometer from Varian Inc. The excitation wavelength is 225 nm and the emission wavelength 338 nm.

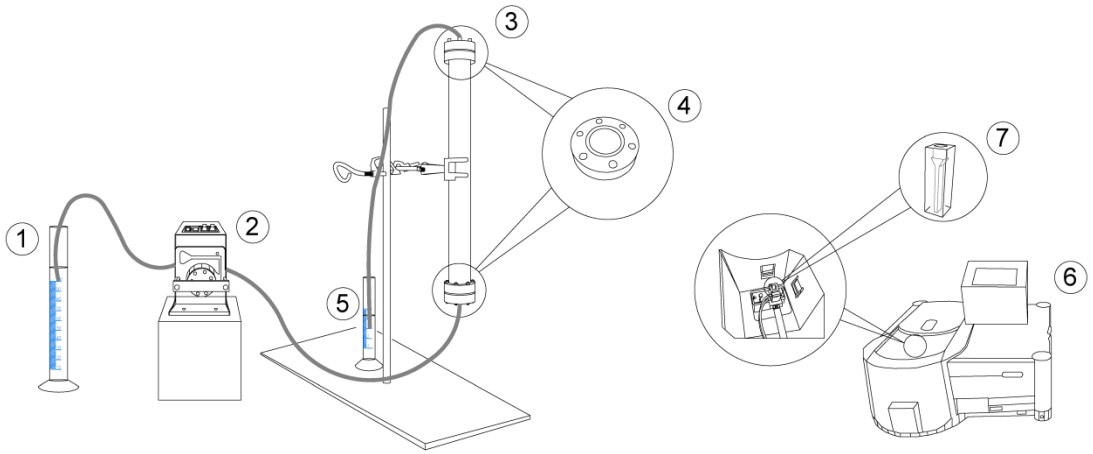

Figure 2: Experimental setup of two-phase flow system. 1) Reservoir of n-octane with KIS tracer. 2) Peristaltic pump. 3) Sand column. 4) Cap embedded with frit. 5) 5ml measuring cylinder. 6) Fluorescence spectrophotometer. 7) High precision fluorescence cuvette.

2.1.2 Porous media

Five porous media – three glass-beads media and two natural sands - are used to investigate the influence of grain-size and texture on n-octane-water interfacial area. The relevant properties of the porous media are described in **Table 1**. Examples of microscopic images of the grains and the grain-size distributions obtained by digital image analysis performed on these images are shown in **Figure 3**. The images were processed using ImageJ software to determine the grain-diameters, roundness, Feret diameter, aspect ratio and circularity (Tatomir et al. 2016a). The three glass-bead porous media are a very fine sand (10-80 μm, $d_{50} = 55\ \mu m$), a fine sand GB170 (120-230 μm, $d_{50} = 170\ \mu m$) and fine-to-medium sand GB240 (160-320 μm, $d_{50} = 240\ \mu m$). GB240 from GRACE (Glass beads 80/60 mesh) is very well sorted with the most uniformly distributed spectrum. The natural-sand porous media can be described as fine sand NS210, (120-320 μm, $d_{50} = 210\ \mu m$) and medium sand NS250 (180-380 μm, $d_{50} = 250\ \mu m$).

The capillary pressure – saturation relationships were determined by mercury-intrusion porosimetry (MIP). To scale the relationships to the n-octane-water system, we used the contact angles, $\theta_{o,w}$, which were determined using digital image analysis (DIA) on microscopic images using the n-octane-water fluid system together with the grains of each porous media (**Table 1**). The conversion of an air-mercury system to an octane-water system is accomplished by rearranging Washburn relationship as given in eq. (1).

$$p_{c_{o,w}} = p_{c_{Hg,a}} \cdot \frac{\sigma_{o,w} \cdot cos\theta_{o,w}}{\sigma_{Hg,a} \cdot cos\theta_{Hg,a}} \qquad (1)$$

where $p_{c_{w,o}}$, $p_{c_{Hg,a}}$, are the capillary pressure for the water-octane fluid system, mercury-air respectively. The mercury – air contact angle $\theta_{Hg,a}$ is 140° and $\sigma_{Hg,a}$ is 480 mN·m^{-1}. $\sigma_{o,w}$, the interfacial tension of water-n-octane is 50.8 mN·m^{-1} at room temperature (Fukunishi et al. 1996).

The curves were fitted to those of the Brooks and Corey (1964) model by minimizing the root mean square error when determining the pore-size index λ, entry pressure p_e, and residual water saturation, S_{wr} in eq. (2):

$$p_c(S_w) = p_d \cdot \left(\frac{S_w - S_{wr}}{1 - S_{wr}}\right)^{-1/\lambda} \quad (2)$$

A high value of the pore index λ corresponds to a flat curve from the entry pressure, S_w=1, until reaching the residual saturation values, indicating the medium is well-sorted and implicitly the pore-throats are of similar size.

Analogously to the uniformity coefficient for grain size distributions, we propose a uniformity coefficient for the pores, defined as the ratio of $C_{pu} = p_{60}/p_{10}$, where p_{60} and p_{10} are the pore diameters corresponding to 60% and 10% finer on the cumulative pore-size distribution curve. A low C_{pu} signifies that the medium is composed of similar pore sizes, equivalent to being well-sorted. **Figure 4**a investigates the relationship between the mean pore diameter, p_{50}, the C_{pu} and the d_{50}. **Figure 4**b shows that the SSSA decreases almost linearly with the mean pore diameter. The distributions of the pores in each of the five materials are determined with mercury intrusion porosimetry, by applying the Washburn equation. The frequencies and cumulative distributions of the pore-size distributions are plotted in **Figure 5**. The glass beads are spherical and of uniform diameter and therefore, the theoretical specific solid surface area can be calculated using the smooth-sphere assumption expressed in (cm^{-1}) using eq. (3) or in (m^2/g), using eq. (4), (Costanza-Robinson and Brusseau 2002; Peng and Brusseau 2005):

$$GSSA(cm^{-1}) = \frac{6(1-\phi)}{d_{50}} \quad (3)$$

$$GSSA\ (m^2/g) = \frac{6}{d_{50} \cdot \rho_p} \quad (4)$$

where d_{50}, is the mean particle diameter (cm), ρ_p is the particle density which is 2.65 g cm^{-3}.

The theoretical total interfacial areas can be estimated based on geometrical calculations for smooth spheres and compared to the specific solid surface areas measured with the MIP method, SSSA-MIP.

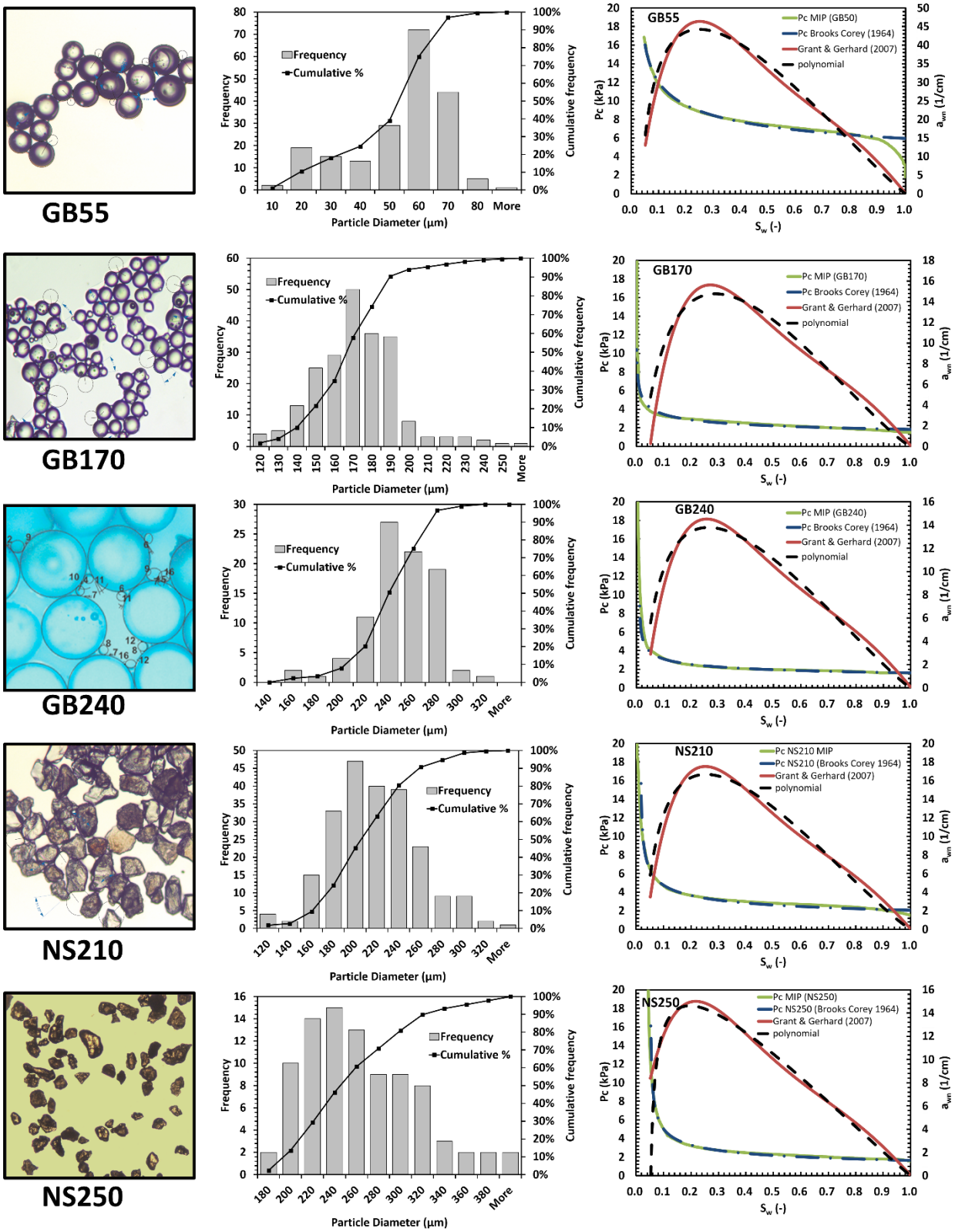

Figure 3: Characterization of the five porous media used in the KIS tracer experiments: three glass beads (GB55, GB170 and GB240) and two natural sands (NS210 and NS250). Digital illustration of the media (left column), grain-size (distribution) with the

cumulative frequency curve (middle), capillary pressure-saturation, $p_c - S_w$ relationship determined with MIP, and the calculated $a_{wn} - S_w$relationship with the explicit interfacial area model of (Grant and Gerhard 2007)

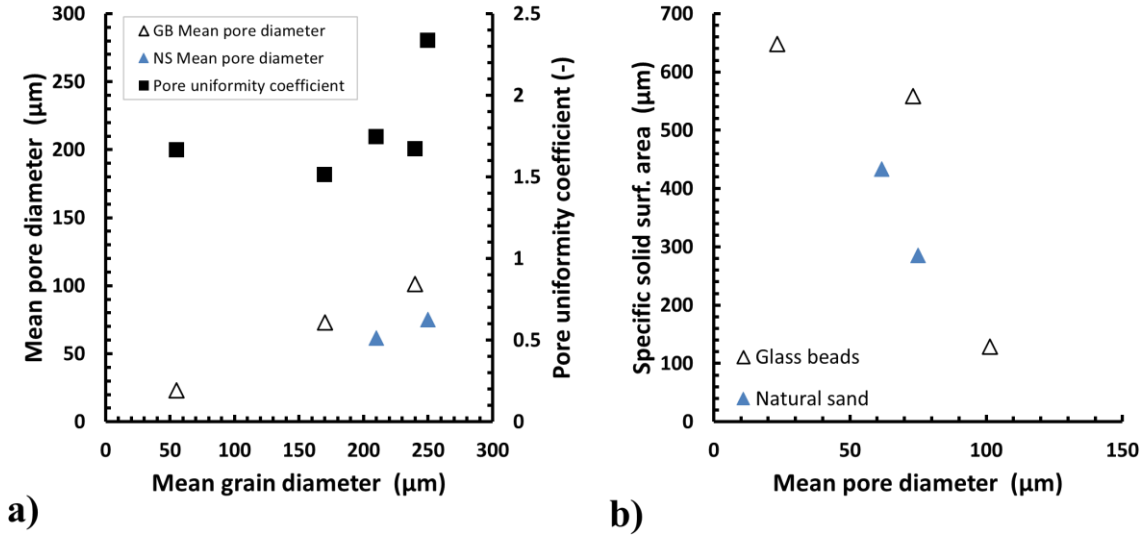

Figure 4: a) Relationship between mean pore-throat diameter (measured with MIP), p_{50}, pore uniformity coefficient ($C_{pu} = p_{60}/p_{10}$) and the mean grain diameter (measured with DIA), d_{50}; **b)**The upper p_{50} values at GB55 and NS250 are corrected to remove the micro-porosity determined with MIP.

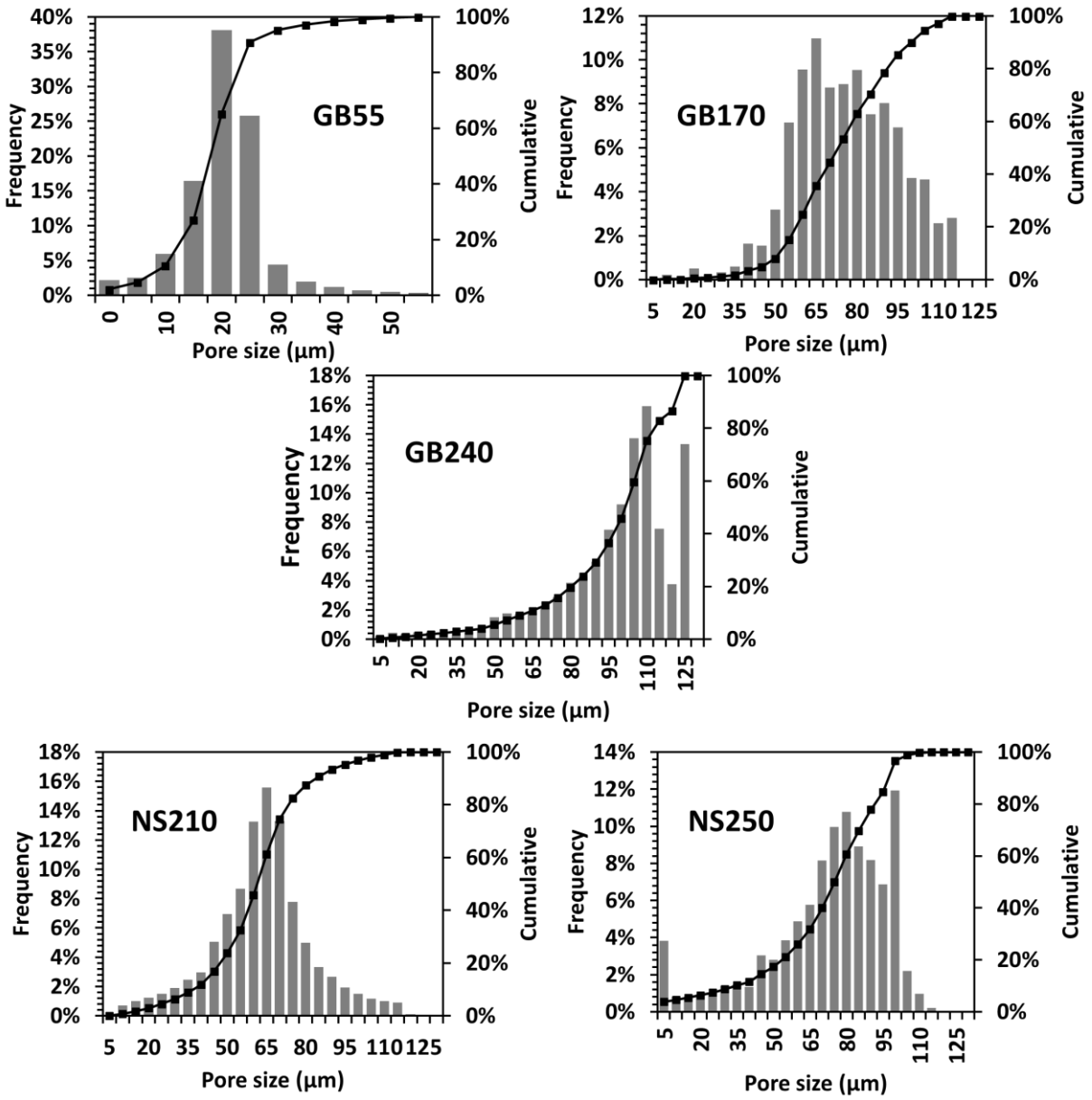

Figure 5: Pore-diameter distribution determined with mercury-intrusion porosimetry, based on Washburn model (Washburn 1921)

Table 1. Summary of relevant properties of the porous media used in the KIS tracer two-phase flow experiments

Parameter Name	Unit	Symbol	GB55	GB170	GB240	NS210	NS250
Porosity	$(-)$	ϕ	0.411	0.455	0.464	0.432	0.445
Intrinsic permeability	(m^2)	K	8e-13 – 2e-12	4e-12 – 1.1e-11	8e-12 - 1e-11	6e-13 – 8e-13	3e-12-9e-12
d_{50} mean grain diameter	(μm)	d_{50}	55	167	240	206	248
d_{10}	(μm)	d_{10}	20	140	205	161	198

d_{60}	(μm)	d_{60}	57	172	244	214	258
Uniformity coefficient $C_u = d_{60} / d_{10}$	$(-)$	C_u	2.85	1.23	1.19	1.33	1.30
Mean pore diameter[a]	(μm)	p_{50}	23.28	73.15	101.35	61.69	75.01
Pore uniformity coefficient[a] $P_u = p_{60} / p_{10}$	$(-)$	P_u	1.67	1.51	1.67	1.75	2.34
SSSA- MIP (Rootare and Prenzlow 1967)	(cm^{-1})	a_s	615	558	128	419	274
GSSA=$6(1-\phi)/d_{50}$	(cm^{-1})	a_s	643	196	134	165	134
Bulk density of the glass beads	(g/cm^3)	ρ_b	1.65	1.65	1.6	1.65	1.67
Lambda (Brooks-Corey)	$(-)$	λ	3.614	3.606	3.650	2.925	2.663
Contact angle n-octane - water	(°)	θ	32± 6	34± 9	10 ± 3	32± 10	32± 10
Entry pressure	(Pa)	p_d	5937	1819	1606	2050	1642
Residual wetting phase saturation	$(-)$	S_{wr}	0.024	0.00	0.016	0.015	0.051
Longitudinal dispersivity	(m)	α_L	1e-3	1e-3	1e-3	1e-3	1e-3
Transversal dispersivity	(m)	α_T	1e-5	1e-5	1e-5	1e-5	1e-5
Feret diameter(mm)	(mm)		0.054	0.173	0.24	0.245	0.273
Circularity	$(-)$		0.857	0.855	0.898	0.676	0.593
Aspect ratio	$(-)$		1.062	1.065	1.018	1.457	1.59
Roundness	$(-)$		0.95	0.955	0.983	0.713	0.701

[a] Based on mercury intrusion porosimetry measurements

Table 2: Fluid and soil-fluid properties

Parameter Name	Unit	Symbol	Value/ Range
Diffusion coefficient	(m^2/s)	D_m	1e-9
Density water	(kg/m^3)	ρ_w	1000
Density n-octane	(kg/m^3)	ρ_n	703
Viscosity of water	$(Pa \cdot s)$	μ_w	1.00e-03
Viscosity of n-octane	$(Pa \cdot s)$	μ_n	5.42e-04
Surface tension n-octane - water[a]	(N/m)	$\sigma_{o,w}$	0.0508
Longitudinal dispersivity[b]	(m)	α_L	1e-3
Transversal dispersivity	(m)	α_T	1e-5

[a] Measurements of surface tension determined by capillary rise method showed no differences between pure n-octane and n-octane with 2g/l dissolved KIS tracer

[b] Measured by single-phase tracer experiments in the column

2.2 Methods

In this study the KIS tracer method is used to quantify the FIFA in several unconsolidated porous materials. The KIS tracer experimental procedure was developed and described in Tatomir et al. (2018). The technique consists of transient drainage experiments of an initially fully water saturated porous media filled column. The drainage/invading fluid is n-octane with KIS tracer dissolved in it. The laboratory experimental outcomes are volumetric outflow BTCs and KIS tracer reaction product in water phase, i.e., 2-NSA concentration BTCs.

2.2.1 KIS tracers

KIS tracers, developed by Schaffer et al. (2013), are a category of non-polar, hydrolysable phenolic esters. In contact with water they undergo an irreversible reaction at the fluid-fluid interface to form two highly soluble products, i.e., an acid and an alcohol, Eq. (5). Their non-polarity allows KIS tracers to be dissolved in non-polar liquids, e.g., n-octane. Due to the pronounced fluorescent properties of their reaction products, the detection is performed by a fluorescence spectrophotometer.

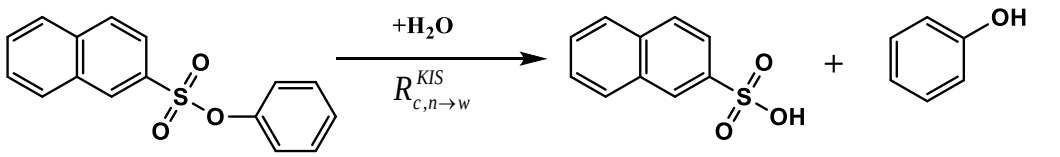

(5)

Phenyl Naphthalene-2-Sulfonate
λ = 280 nm → 343 nm

Naphthalene-2-Sulfonic Acid
λ = 225 nm → 338 nm

Phenol
λ = 269 nm → 296 nm

where $R_{c,n\rightarrow w}^{KIS}$, is the reaction rate constant, determined in static batch experiments.

The KIS tracer method was developed for tracking the FIFA in dynamic conditions (Tatomir et al. 2018). Explicitly, the method is developed for the primary drainage process, i.e., non-wetting phase displacing the wetting phase in a proof of concept study using well-characterized glass beads in well-controlled laboratory conditions. By interpreting the volumetric ratios at outflow and the reacted KIS tracer product acid breakthrough curves, we can derive the specific IFA relationship of the fluid-fluid-porous media system.

Note that the 2-NSA mass reacted in pendular rings of wetting fluid, around the contact points of the porous media, cannot leave the column and is not being measured. Only the fraction of the fluid-fluid interface belonging to the terminal menisci in contact with the continuous wetting fluid body or mobile part is quantified by the KIS tracer technique.

2.2.2 Kinetics of the tracer, new insights

The KIS tracer hydrolysis reaction at the fluid-fluid interface was shown in static batch experiments to lead to a linear increase of concentration after about 2000 – 3000 minutes (Schaffer et al. 2013), independent on the initial KIS tracer concentration in the non-wetting phase, i.e. n-octane. However, at the early stage (up to 100-200 minutes) was observed that the reaction rate is increasing linearly depending on the initial concentration of the KIS tracer in the non-wetting phase (**Figure 6**). With the pumping rates ranging between 0.3 and 1.5 ml/min one column experiment usually takes around 6000 seconds. Therefore, the kinetic rates of the experiment are the ones represented in **Figure 6**b). Generally, a higher reaction rate is preferable to obtain higher 2NSA concentrations in water, because they can be better detected and measured with the fluorescence spectrophotometer. Using an initial concentration of 2g/l KIS tracer, we extend our previous range of testing which was 1g/l (Tatomir et al. 2018). It can be observed that the resulting kinetic rate coefficient $R_{n\rightarrow w}^{2NSA}$ =1.25 10^{-11} kg·m^{-2}·s follows very well the linear behavior.

In this study, the experiments are conducted with an initial concentration of 0.5 g/l (all experiments with GB55 and NS210, and two of the experiments with GB170) and 2g/l (all experiments with GB240 and NS250 and one experiment with GB170) (**Figure 8**). Note that the

previous study (Tatomir et al. 2018) was conducted with the GB240 glass-bead medium with an initial KIS tracer concentration of 0.5g/l.

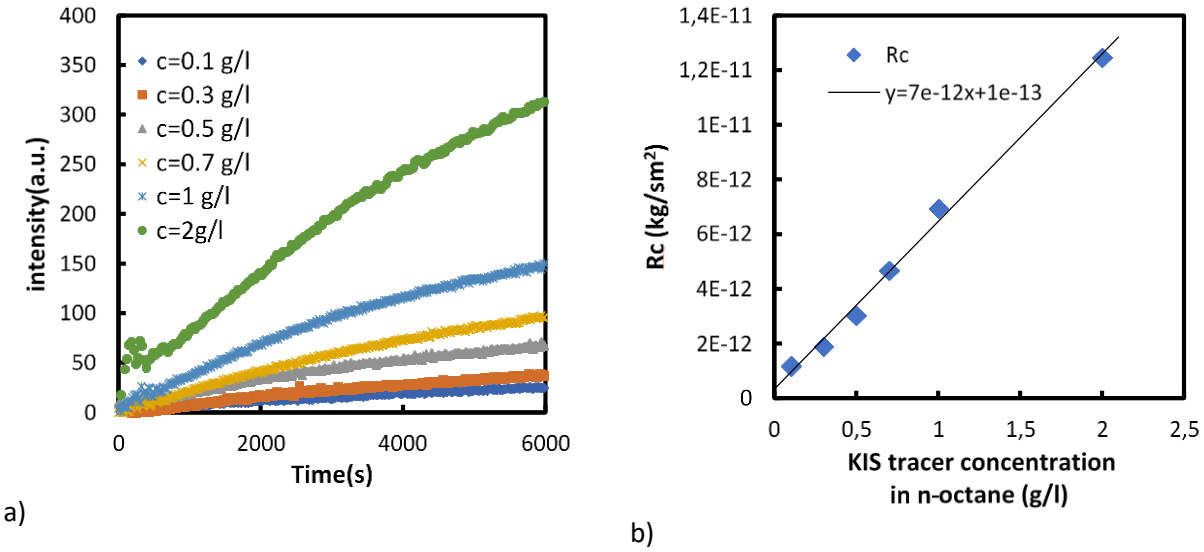

Figure 6: Measured kinetic rates in static batch experiments. a) 2-NSA concentration reaction rates over time expressed in intensity units as a function of initial 2-NSAPh concentration in n-octane. b) calculated hydrolysis reaction rates as a function of initial 2-NSAPh concentration using the experiments in subfigure a). Here the unit of intensity $a.u = 86.293 \cdot c_{2NSA} + 62.6$

The hydrolysis reaction is expressed as:

$$-\frac{dc_\alpha^\kappa}{dt} = r_{n\to w}^\kappa = R_{c_{n\to w}}^\kappa \cdot a_{wn} \,, \tag{6}$$

where c_α^κ is the concentration of component κ in phase α, $R_{c_{n\to w}}^\kappa$ is the reaction rate constant. For component 2-NSA in water phase, $R_{c_{n\to w}}^{2NSA}$ was determined in static batch experiments (Figure 6). The a_{wn} is the capillary associated IFA. According to Joekar-Niasar and Hassanizadeh (2012) a_{wn} can be expressed using the polynomial expression in Eq. (7):

$$a_{wn}(S_w, p_c) = a_0(S_w)^{a_1}(1 - S_w)^{a_2}(p_c^{max} - p_c)^{a_3} \tag{7}$$

where a_{wn} is the capillary associated IFA, S_w is the wetting saturation, p_c is the capillary pressure, $a_0, a_1, a_2, a_3, p_c^{max}$ are empirically fitted parameters.

The transport of hydrolyzed KIS tracer in water, i.e. 2-NSA, is controlled by advection and diffusion processes.

2.2.3 NAPL-Water Experiments

The steel-column was packed with dry granular material (i.e. sand, or glass beads) using slight vibrations while packing to ensure uniform bulk properties. After packing the column is slowly filled with water from the bottom to avoid air entrapment. The columns are saturated for more

than 24 hours by pumping deaired ultra-pure deionized water. The porous medium properties are reported in Table 1.

The 2-NSAPh (non-polar hydrolysable phenolic ester, phenyl naphthalene-2-sulphonate) in concentrations of 0.5 g/l and 2g/l in the n-octane, is used as the KIS tracer. Approximately 30 ml of the solution is then injected into the column at a rate between 0.4 and 0.8 ml/min. At the outlet the two-phase flow breakthrough curve (BTC) was captured by collecting the fluid volumes in 5 ml graded measuring cylinder. Using a glass syringe, the water containing reacted KIS tracer is taken and placed in a 500 µl cuvette to be analyzed in the spectrophotometer. A predefined calibration curve allows the conversion of intensity readings into 2-NSA concentration (**Figure 6**). After the analysis, the water is collected in 5-ml vials. Initially, at the outlet, only water is being drained from the system. Just before the arrival of the first n-octane at the outlet, the sampling intervals are taken more often for a higher temporal resolution of the BTC. The sampling frequency is dictated by the minimum volume of water required to fill the cuvette that is placed in the spectrophotometer.

After every experiment the glass beads and the natural sands are washed and dried for more than 48 h. The porous steel frits of the columns are washed and dried before each experiment and the packing process repeated. However, each packing will lead to a different grain geometric configuration, which may lead to differences in petrophysical parameters, i.e. permeability, tortuosity with little influence on porosity.

2.2.4 Data analysis: Mathematical modelling and interpretation of the results

The interpretation of the experimental results is done using numerical modeling. The mathematical and numerical model to handle the column-scale, i.e. Darcy (REV) scale, is an immiscible two-phase flow model with reactive transport and it accounts for the specific IFA (Tatomir et al. 2018). The mathematical model is implemented in COMSOL Multiphysics v5.5. Several models capable of addressing the KIS tracers in multiphase flow in porous-media systems were developed in the past (Tatomir et al. 2013; Tatomir et al. 2015; Tatomir et al. 2016b; Tatomir et al. 2018). Besides the immiscible two-phase flow models, a compositional model investigating the KIS tracer application in supercritical CO_2 – brine fluid systems was developed in the DuMu^X simulator (Flemisch et al. 2011; Tatomir et al. 2015). Comparing the two models applied with experimental data, Tatomir et al. (2018) showed only minor differences. In this study, the results were interpreted with the COMSOL implemented model only.

A two-step approach is employed to interpret the results. The first step is the calibration of the two-phase flow model to the experiment by performing a sensitivity analysis with respect to flow rate, Q, and intrinsic permeability, K. It is estimated that both have the highest measurement uncertainty, due to the expected small oscillations in the pumping rate (±0.05 ml/min) and the unknown influence of repacking the columns, and of the column frits. The peristaltic pump is set to operate at a fixed number of rotations per minute. As pressure in the column and the n-octane reservoir at the inlet changes during the experiment, flow rate fluctuations can be expected. The permeabilities of the sand are determined by falling head permeameter, which may provide a wide range of permeability values. Adding to the uncertainty of the permeability measurement is the effect of the porous frits and of repacking before each experiment.

Once the outflow volume ratio curves are matched, we proceed with the calibration of the concentration breakthrough curves of the KIS tracer reaction product, i.e. 2-NSA. In this sense, a sensitivity analysis using the specific interfacial-area relationship, $a_{wn} - S_w$, as the unknown parameter is conducted. The reaction rate expressed in Eq. (6) depends on the reaction rate coefficient, known from experiments and on a_{wn}. Initially, the Grant and Gerhard (2007) thermodynamically derived model is used to approximate the specific IFA a_{wn} curves from the MIP measured $p_c - S_w$ relationships. Afterwards, the polynomial expression in Eq. (7) is used to fit the modelled a_{wn}, by finding best fitting parameters,a_0, a_1, a_2, p_c^{max}. This provides the theoretical $a_{wn} - S_w$ of the fluid-fluid porous medium system.

The second step comprises the calibration of the KIS reaction product breakthrough curves. This is performed running a parameter sweep on parameter a_0 in Eq. (7). This parameter controls the maximum specific IFA, a_{wn}^{max} while maintaining the general shape of the $S_w - a_{wn}$ curve.

The solute dispersivities were determined using fluorescent tracer experiments to be 10^{-3} m (Tatomir et al. 2018). Note that dispersivities measured in single-phase flow conditions is not necessarily valid when another fluid-phase is present (Karadimitriou et al. 2016). Applying the root mean square error (RMSE) as a criterion the best fitting curves were found.

In order to compare with the experimental and modelling BTC curves, the modelling results are post-processed. The volumetric ratios of the non-wetting phase to total fluid measured at the outlet are integrated over the sampling intervals, to obtain the values at the times when the samples were taken. For further details of the mathematical models, see Tatomir et al. (2018) proof of concept study.

3 Results

The experimental and modelling results for the three sets of tests performed on each of the five porous media, three glass beads, GB55, GB170, GB240, and two natural sands, NS210, NS250, are presented in section 3 and discussed in section 4.

3.1 Two-phase flow calibration

All fifteen experimental breakthrough curves (BTCs) of the volume fraction of the non-wetting phase to total fluid volume together with the model calibration BTCs are illustrated in **Figure 7**. The modelling parameters determined from the petrophysical characterization of the natural sands and glass beads samples are reported in Table 1 and of the fluid system in Table 2.

First, we calibrate the immiscible two-phase flow model by performing the parameter sweep with a combination of flow rates and permeabilities. The fitting of the modelling results to the experimental data is shown in **Figure 7**. It can be observed that the two-phase flow model can well match the experimental breakthrough curve, with the root mean square errors ranging up to 0.057 for the best fitting model curves, as showed in **Table SI 1**. Deviations are found mainly in two experiments performed with GB170, where the change in the non-wetting to total volumetric ratio at breakthrough is gentler in the experimental data compared to that of the modelled

breakthrough. In contrast, for NS210, the non-wetting phase breakthrough is fast and only little water volume is being displaced out of the column, leading to a smaller number of data points. This becomes apparent in the increase of non-wetting to total volume ratio at breakthrough occurring more rapidly in the experimental BTC than the modelled ones.

Even though the frits are washed and dried before each experiment and the packing processing follows the exact same procedure (vibrating and adding small increments) for each experiment, differences are hard to avoid. The reproducibility of the experiments is mainly affected by repacking and by the frits condition, which are reflected by the overall permeability of the system. Therefore, the calculated flow rates and permeabilities in **Table SI 1** for the three experiments belonging to each sand category are slightly different.

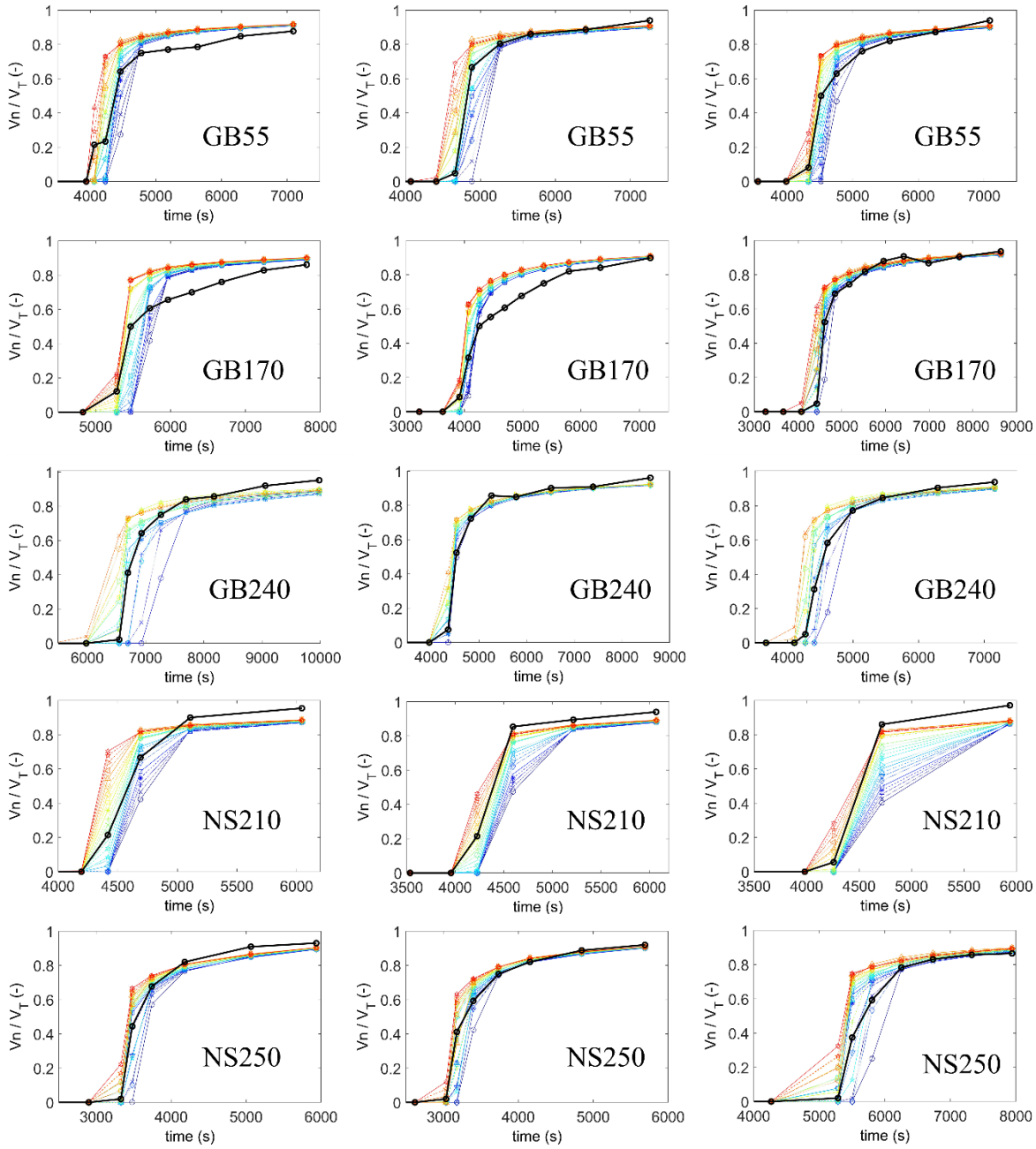

Figure 7: Breakthrough of the volumetric fraction of non-wetting phase to total fluid volume at the column outlet, experimental data (black) and simulated breakthrough curves with sensitivity analysis (color). The variation ranges are provided in **Table SI 1**

3.2 Interpretation of the hydrolyzed KIS tracer reaction product breakthrough curves

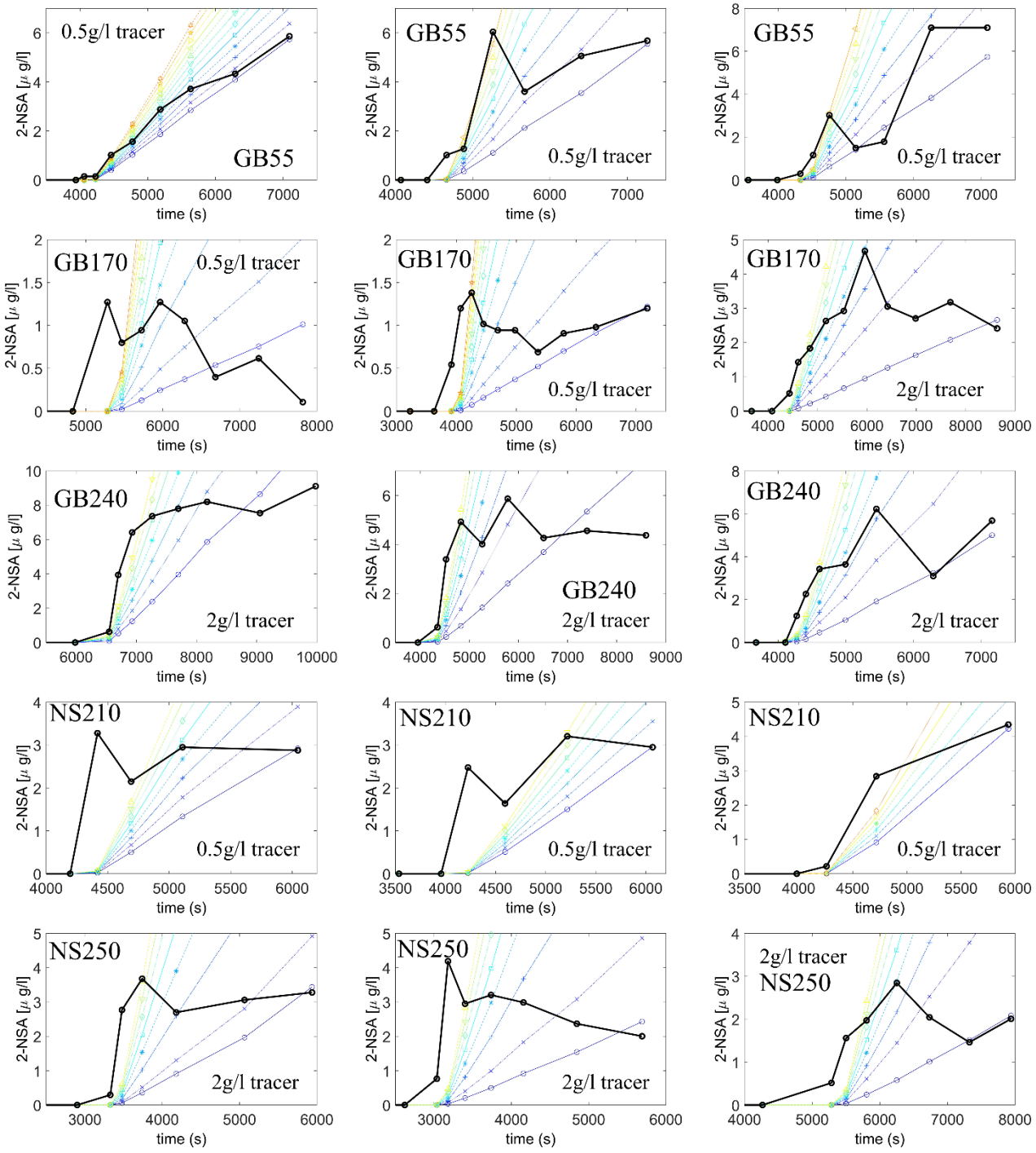

Figure 8: Breakthrough curve of 2-NSA concentration (hydrolyzed KIS tracer) at column outlet. The black curve shows the experimental-data, while the colored plots correspond to a range of fitting coefficient a_0, varied between $a_{0,min}$ and $a_{0,max}$ (yellow) given in **Table 3**. The initial KIS tracer concentration in n-octane is specified in each subfigure

Table 3: Parameters ranges, $a_{0,min}$ to $a_{0,max}$ used to identify the best fitting for the capillary-associated IFA, a_{wn} in Eq. (7). Here $a_{0,GG}$ and $a_{0,BF}$ are the a_0 parameter best fit to the Grant and Gerhard (2007) model, and to the experimental data

Soil category	$a_{0,min}$	$a_{0,max}$	$a_{0,GG}$	$a_{0,BF}$	a_1	a_2	a_3	p_c^{max} (Pa)
GB55	9.67×10^{-6}	4×10^{-5}	5.22×10^{-5}	1.33×10^{-5}	0	1.11	1.94	23287
GB170	4×10^{-6}	7.33×10^{-5}	5.23×10^{-5}	6.67×10^{-6}	0	1.21	2.18	5749
GB240	1×10^{-5}	8×10^{-5}	5.31×10^{-5}	$1.33e\times10^{-5}$	0	1.15	2.14	5804
NS210	3.5×10^{-6}	8.5×10^{-5}	5.95×10^{-5}	4.33×10^{-5}	0	1.15	2	9466
NS250	5.33×10^{-6}	6×10^{-5}	6.06×10^{-5}	6.33×10^{-6}	0	1.05	1.83	15491

The breakthrough curves of the reacted 2-NSA concentration are plotted in Figure 8. Measured 2-NSA concentrations in water range between 0 and 8 µg/l. With a constant kinetic rate dependent on the initial tracer concentration in n-octane (Figure 1), the mass transfer across the fluid-fluid interface is a function of only fluid-fluid interfacial area. In order to obtain the range of the specific interfacial area when fitting to the experimental data, the parameter a_0 in the polynomial equation (7) is swapped to change the magnitude of the $a_{wn} - S_w$ curve while maintaining the shape of the curve (Tatomir et al. 2018). The calculated root mean square error ranges between 0.3 and 2.3 for the best fitting parameter a_0, as shown in **Table SI 1**. Compared to the non-wetting phase fluid to total volume ratio BTCs calibration, the modelled 2-NSA BTCs have a larger deviation from the experimental data. Generally, the trend of the BTCs is ascending. However, a clear linearly increasing trend, as it is predicted by the numerical models, is not always seen in the experimental data. This indicates that either we deal with a systematic experimental error, or the theoretical framework underlying the current coupled two-phase flow and reactive-transport model needs to be reconsidered. This is further addressed in the discussion.

3.3 Capillary-associated specific interfacial area calculation

The range of the $a_{wn} - S_w$ curves and the best fitting curves found for the five porous materials are illustrated in Figure 9 with gray shading. The gray shading corresponds to the range of a_0 values (Table 3) that scale the $a_{wn} - S_w$ curves so that all experimental data points of the 2-NSA BTCs in Figure 8 are captured. The maximum $a_{0,max}$ values correspond to the peak matching the first points on the BTC, the curve with steepest slope, while the minimum, $a_{0,min}$, corresponds to the curves matching the points on the tailing of the BTC. Once a_0 is determined, the a_{wn}^{max} value can be obtained from the $a_{wn}(S_w)$ curve, which usually exists at water saturation ranging between 0.2 and 0.35. The best fitting $a_0$values, $a_{0,BF}$, obtained on grounds of RMSE are given in **Table SI 1** together with the a_{wn}^{max} and the RMSE values and are plotted in Figure 10.

The a_{wn} predicted by the explicit IFA model of Grant and Gerhard (2007), using the MIP $p_c - S_w$ curves is within the areas resulting from the interpretation of the 2-NSA tracer breakthrough curves, for all grains, except for the natural sand NS250. In this case, the Grant and Gerhard (GG) model overestimates the a_{wn}. Generally, the GG model provides larger FIFA than

those providing the best fit resulting from the tracer interpretation. For NS210 the best fit of the third experiment matches almost exactly the GG model. On average the GG model predicts a_{wn} values that can be even five times larger than those obtained for the model best fits.

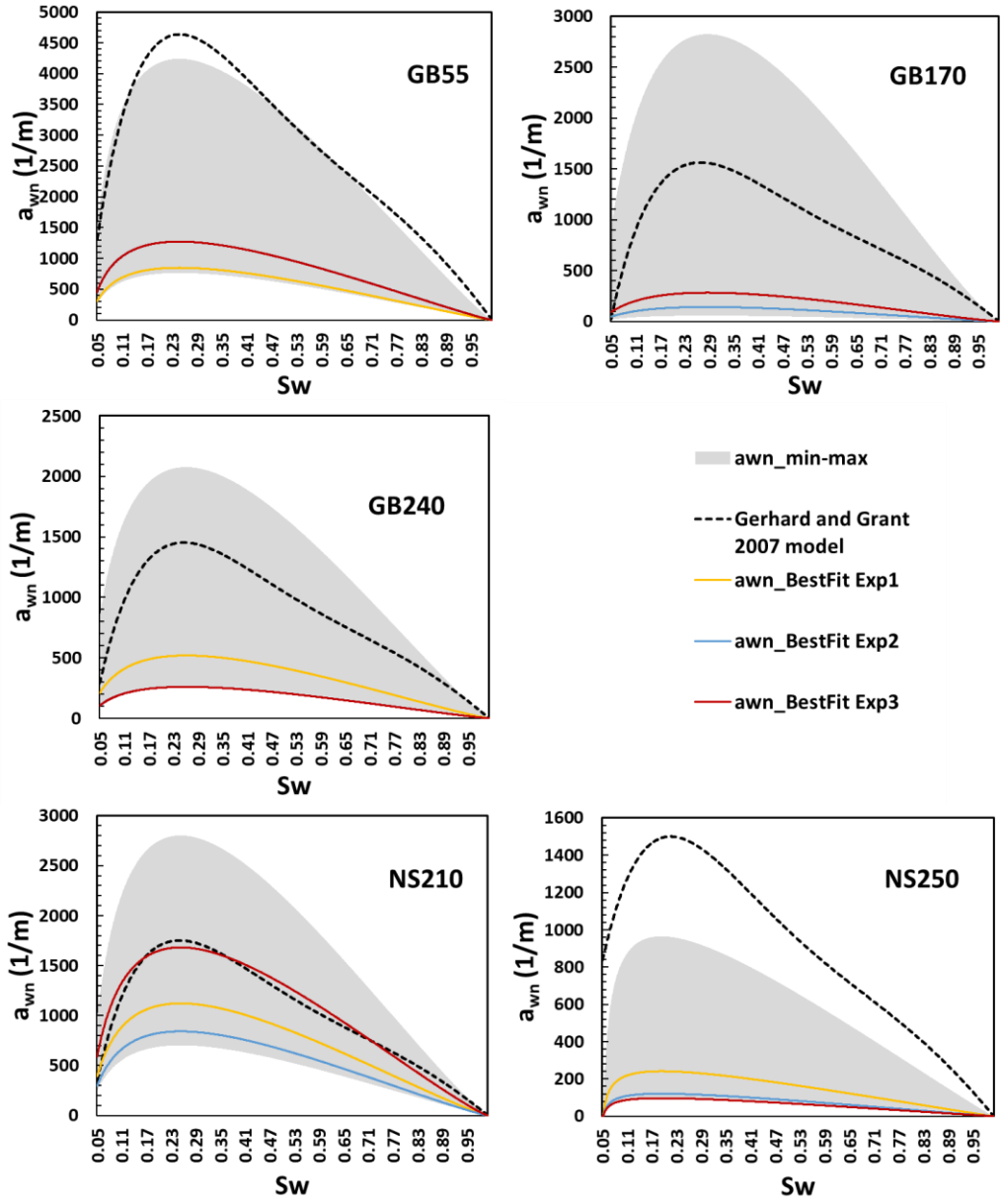

Figure 9: Ranges for the specific capillary associated IFA, $a_{wn} - S_w$ relationships, for the five porous media. The best fitting curves in each experiment (Exp.1 - yellow, Exp.2 - blue, Exp.3 - red), and the Gerhard and Grant model applied to MIP derived $p_c - S_w$ curves

4 Discussion

Assuming two fluid phases inside the porous medium as being stagnant. Since there is no force applied, the IFA between the fluids remains constant and the KIS tracer hydrolysis over the fluid-fluid interface produces a steady increase of the 2-NSA concentration in water. As time passes,

the 2-NSA concentration diffuses away from the fluid-fluid interface with the only driving force of the process being the concentration gradient, i.e., molecular Brownian motion. When the non-wetting phase starts to displace the wetting phase, a transition zone is formed, where saturation changes with time. During this process, only the tracer concentration in water in direct proximity to the outflow is measured. In other words, only the interfaces belonging to the front can contribute to the measured concentration at the outlet. The longer the two fluids remain in contact the higher the outlet concentration should be. In reality, the pore distribution inside the column forms complex geometrical patterns. The macro-scale displacement front is in fact formed of fingers following various tortuous pathways.

Therefore, an early arrival of the concentration peak corresponds to a larger number of fingers arriving at the outlet, which are followed by other fingers that are halted due to the presence of a confinement in the pore space, and the competitive domination of fingers occupying smaller pores than the first ones that, combined, result in a lower outlet concentration. Some of the fingers may also mobilize water in the capillaries which may eventually be pushed to regions that are stagnant. In these regions the advective transport flux is almost zero. The water in these regions never reaches the outlet and, implicitly, the corresponding concentration is never measured. Visualization of the mobile and immobile zones can be done for instance in thin transparent (quasi-) two-dimensional micromodels (Karadimitriou et al. 2016). In a few words, the effects taking place on the pore scale can and will affect the corresponding outflow concentration and, given the experimental setup, it is physically impossible to identify the pore-scale filling sequence mechanism.

The immiscible displacement can be studied as a function of the capillary number, $Ca = v\mu_i/\sigma$ and the viscosity ratio $M = \mu_i/\mu_d$ (Lenormand et al. 1988), where v is the velocity of the invading fluid, μ_i and μ_d are the dynamic viscosities of the invading and displaced fluids, and σ is the interfacial tension between the two fluids. A stable front means that the transition zone (width) is constant in time. If the displacing or the invading fluid is less viscous than the displaced fluid the front tends to become unstable. In our case $M = 0.5$ and the Ca of the fifteen experiments is between 0.4 and 3.5 (Appendix SI Table 1). When M gets smaller, preferential flow starts to occur, increasing the lengths and widths of the transition zone (e.g., Heiß et al. 2011). For the KIS tracer experiments, a stable front having a narrow transition zone will lead to fewer measurement points than compared to those induced by an unstable flow with a large transition zone. The NS210 experiments have the highest Ca numbers, 2.58, 2.7 and 3.6 while the NS250 the lowest, i.e., 0.34, 0.59 and 0.62 (**Table SI 2**). For NS210 the BTCs have maximum 4 measurements, while in for NS250 the minimum number of points is 6.

4.1 Hydrolyzed KIS tracer breakthrough curves

Examining the 2-NSA breakthrough curves in **Figure 8**, the two main differences between modelled and experimental results are: First, after phase breakthrough for most of experiments (11 out of 15), the BTCs exhibit an early concentration peak immediately after the first arrival,

usually within the first three sampling times. The second difference is the deviation of the experimental BTC from a straight line. They have a non-linear behavior characterized by a slower increase in concentration, or even by a decrease at late times (i.e., first experiment GB170, second experiment NS250). The concentration peak and the concentration decrease are not present in the BTC predicted by the models but the breakthrough curves appear as straight lines. In fact, such effects cannot be reproduced by our current model. Closest to the predicted linear trend of the reactive transport model are the BTCs for the GB55. The curves consist of more than 6 measurement points.

With the lowest grain-uniformity coefficient, C_u, value of 1.19, GB240 is the most uniform medium, closest to an ideal mono-size medium. RMSE values for of the GB240 obtained when matching the volumetric ratios BTCs during the two-phase flow model calibration are the lowest of the five materials. The three GB240 experiments are conducted with an initial KIS tracer concentration of 2g/l. The same glass beads were used in our previous study (Tatomir et al. 2018), where we ran four experiments with an initial KIS tracer concentration of 0.5 g/l. In comparison to our previous study where the BTCs had maximum four measurement points, the BTCs have now eight measurement points. Two of the four results in (Tatomir et al. 2018) provided a narrow a_{wn}^{max} range, i.e., 4.1 -5.4 cm^{-1} , 5.0 -7.5 cm^{-1}, and the other two large a_{wn}^{max} ranges, i.e. 3.0-15 and 4.6 – 11.5 cm^{-1}. The best fitted results in **Table SI 1** give a_{wn}^{max} ranges between 2.6 – 5.19 cm^{-1} which can be considered in good agreement with our previous set of experiments.

Generally speaking, the confidence in measurements increases when a larger number of measurement points is available. Even though the first GB170 experiment has eight measurement points the BTC presents a clear descending trend, while the other two experiments tend to flatten out.

From Figure 9 the largest a_{wn}^{max}error range, i.e. $a_{wn}^{max}(a_{0,\max}) - a_{wn}^{max}(a_{0,\min})$ is encountered for the GB55, 8.2 - 42.4 cm^{-1}. Excluding the GB55, the natural sands with a larger surface roughness do not have a larger range of a_{wn}^{max} than the glass beads. The calculated IFAs range for natural sands is 13.99 cm^{-1} for NS210, 13.19 cm^{-1} for NS250 is smaller than that of the glass beads, 34.2 cm^{-1} for GB55, 19.55 cm^{-1} for GB170 and 18.2 cm^{-1} for GB240.

4.2 Potential explanations of discrepancies in tracer BTC

The discrepancies between the modelled and experimental results are believed to highlight the complexity of the coupled multiphase flow and reactive transport processes. The shape of 2-NSA concentration BTCs highly depend on the front behavior when it reaches the outlet. Once being at the outlet the non-wetting phase is continuous, while in the domain entrapped regions of wetting fluid were formed. Let us consider the porous medium being as a bundle of capillaries. Those with the largest apertures/radii are the capillaries first invaded by the non-wetting phase in the displacement process. Should these capillaries represent the largest part, it becomes clear why a concentration peak arrives at the beginning of BTC, just ahead of the fluid-fluid interface

reaching the outlet. For a continuum-scale model, assuming the medium as homogeneous, such type of preferential flow will be averaged.

An early breakthrough peak and other discrepancies could also be explained by artefacts resulting from injection and sampling procedures. Concentration ranges are small, below 10 µg/l, i.e., experimental errors could also be expected. Care was taken when conducting the experiments and several procedures were tried and repeated, and therefore, we do not consider experimental errors and artefacts as a likely reason for the discrepancies.

The parametric study on a_0 values used to scale the $a_{wn} - S_w$ curves covers all experimental data points of the 2-NSA BTCs in Figure 9. Therefore, it is reasonable to assume that one of the $a_{wn} - S_w$ represents the "true" solution. One can see that the theoretical model of Grant and Gerhard (2007) is in four cases within the parameter range, even providing an exact match for the third experiment with NS210. This indicates the specific IFAs measured with KIS tracer method are within a reasonable range.

4.3 Grain-diameter-size influence on IFA

Previous literature studies, reviewed in the introduction, revealed that the total specific IFA, a_n, and its related, a_{wn}, are inversely proportional to the mean grain size (Brusseau et al. 2009; Brusseau et al. 2010). They observe very strong correlation between total specific interfacial area and IMGD. Furthermore, a_n, was observed to have a linear dependency on water saturation. It decreases linearly with S_w , $a_n = a_n^{max}(1 - S_w)$, where the a_n^{max} is the maximum total specific interfacial area. The a_n^{max} was shown to be approximately equal with the solid surface area (a_s) (Porter et al. 2010; Brusseau et al. 2010). The value of a_n is shown to be smaller for smooth glass beads and larger for natural sands, or soils, (e.g., Brusseau et al. 2009). The curve is reported to have virtually no hysteresis, somewhat unexpected as since the $a_{nw} - S_w$ curves present hysteresis.

We found that GB55 has a much larger specific interfacial area compared to GB170 and GB240. The largest specific IFA is recorded for NS210. This implies that materials with smaller grain diameters will have larger specific interfacial area.

4.3.1 Determination of maximum specific capillary-associated interfacial area with the KIS tracer method

In Figure 10 the maximum values for specific capillary associated IFA, a_{nw}^{max}, obtained with KIS tracer method are plotted. We plot the three sets of a_{nw}^{max} obtained for each soil category, the average value and the error range corresponding to the minimum and maximum a_0 values. Implementing a linear regression line over the $a_{nw}^{max} - IMGD$ data we obtain the following relation for the glass-beads material:

$$a_{wn}^{max} = 0.0636/d_{50} - 0.4393 \quad (8)$$

Similar to values reported in the literature for total maximum total FIFA, a_n^{max} , the a_{wn}^{max} follows a linearly increasing trend with an increase in IMGD. There is a clear distinction between the

slopes of the linear regression lines of natural sand materials and glass beads. Having a larger surface roughness than the glass beads, the natural sand a_{wn}^{max} has a much larger increase in slope with IMGD.

The capillary-associated IFAs of the five materials determined with the thermodynamically based explicit IFA model (Grant and Gerhard 2007), follow a linear relationship $a_{wn.\ GG}^{max}$ when plotted against the IMGD. In this case no discrepancy between the natural sands and glass beads is observed.

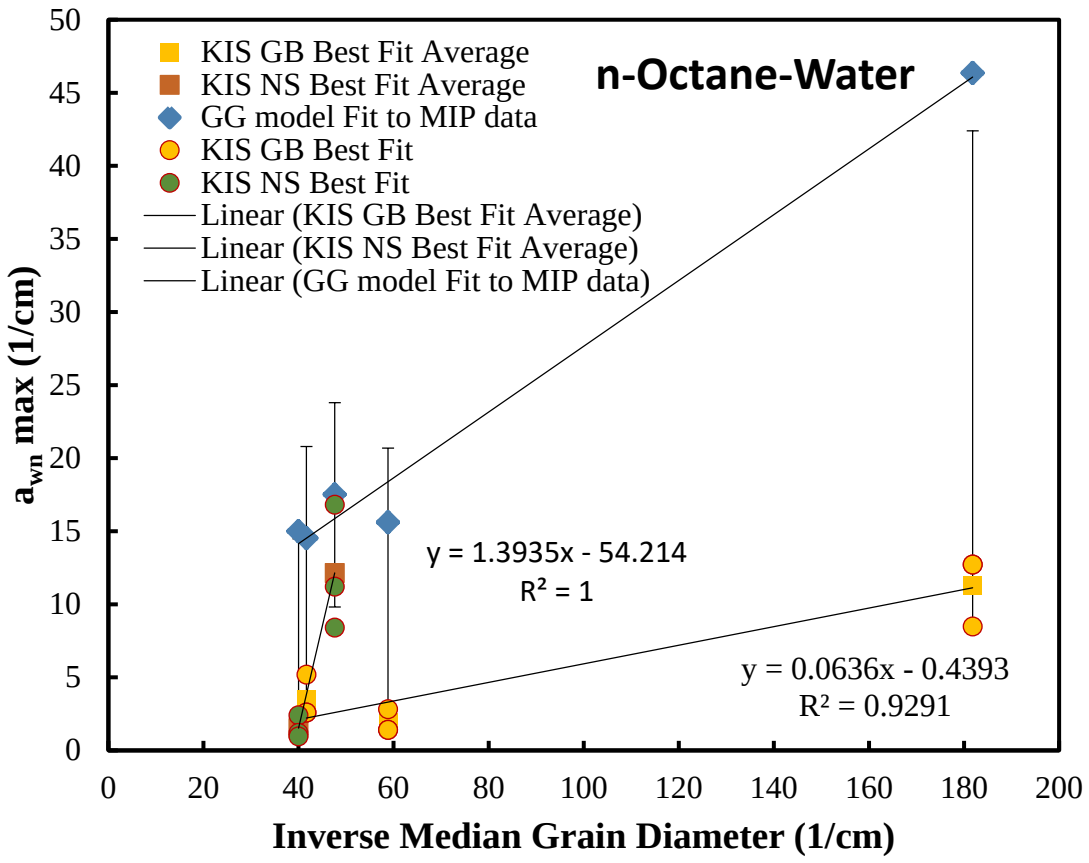

Figure 10: Relationship between n-octane/water maximum specific capillary associated interfacial area, a_{wn}^{max} and inverse median grain diameter. Values determined using the KIS tracers on the five porous media, GB55, GB170, GB240, NS210, NS250. The values for a_{nw}^{max} are reported in **Table SI 1**.

4.3.2 Comparison of maximum capillary associated-specific interfacial area with literature

The comparison of FIFA with the literature data needs to account first for the type of IFA being compared, i.e. total or capillary associated IFA, and for the different porous media-fluid system types. Most commonly, the fluid-systems used in the reported experiments are air-water and, less often, NAPL-water. To the authors' knowledge there are only four studies that report the measured specific capillary associated IFA (Culligan et al. 2006; Brusseau et al. 2006; Porter et al. 2010; Araujo and Brusseau 2020). XMT was used in each of these studies.

Figure 11 plots the a_{wn}^{max} values obtained with the KIS tracer method and with XMT experiments using NAPL-water fluid system from (Culligan et al. 2006; Porter et al. 2010), and air-water fluid system from (Brusseau et al. 2006; Araujo and Brusseau 2020). Likos and Jaafar (2013) developed a pore-geometry model that calculates the specific IFA based on the measured grain-size distributions. They apply their model to four porous media (small glass beads, F75 Ottawa sand, large glass beads, river sand) and plot the capillary-associated IFA, a_{nw}. Note that the capillary-associated IFA determined by Culligan et al. (2006) for air-water and oil-water fluid systems in the same porous medium found the that the capillary-associated IFA for oil-water is larger than that of air-water during main drainage. The surface tension of air-water is higher and the XMT revealed that air phase is located in larger continuous fluid configurations while the oil forms smaller, less well-connected configurations at similar saturations, leading to larger interfacial areas. Here, we do not apply any scaling to a_{wn} values.

It is observed that the literature values plotted against the IMGD, follow a linear trend which is larger than the prediction line of a_{wn}^{max}- IMGD obtained from the KIS tracer experiments. The theoretically determined a_{wn}^{max} values using the (Grant and Gerhard 2007) model (illustrated in **Figure 9**, dashed black curves) are in good agreement with the regression line applied through the literature values. For the n-octane-water fluid system the capillary-associated IFA, a_{wn}^{max} determined by KIS tracers ranges between 3.00 (d_{50}=55 μm) and 4.64 (d_{50}=250 μm) times smaller than the capillary associated IFA reported in the literature. The explanation for this behavior is that the KIS tracer method only measures the mobile fraction of the fluid-fluid interface, which correspond to the mobile terminal menisci displacing the water in the system(Figure 1).

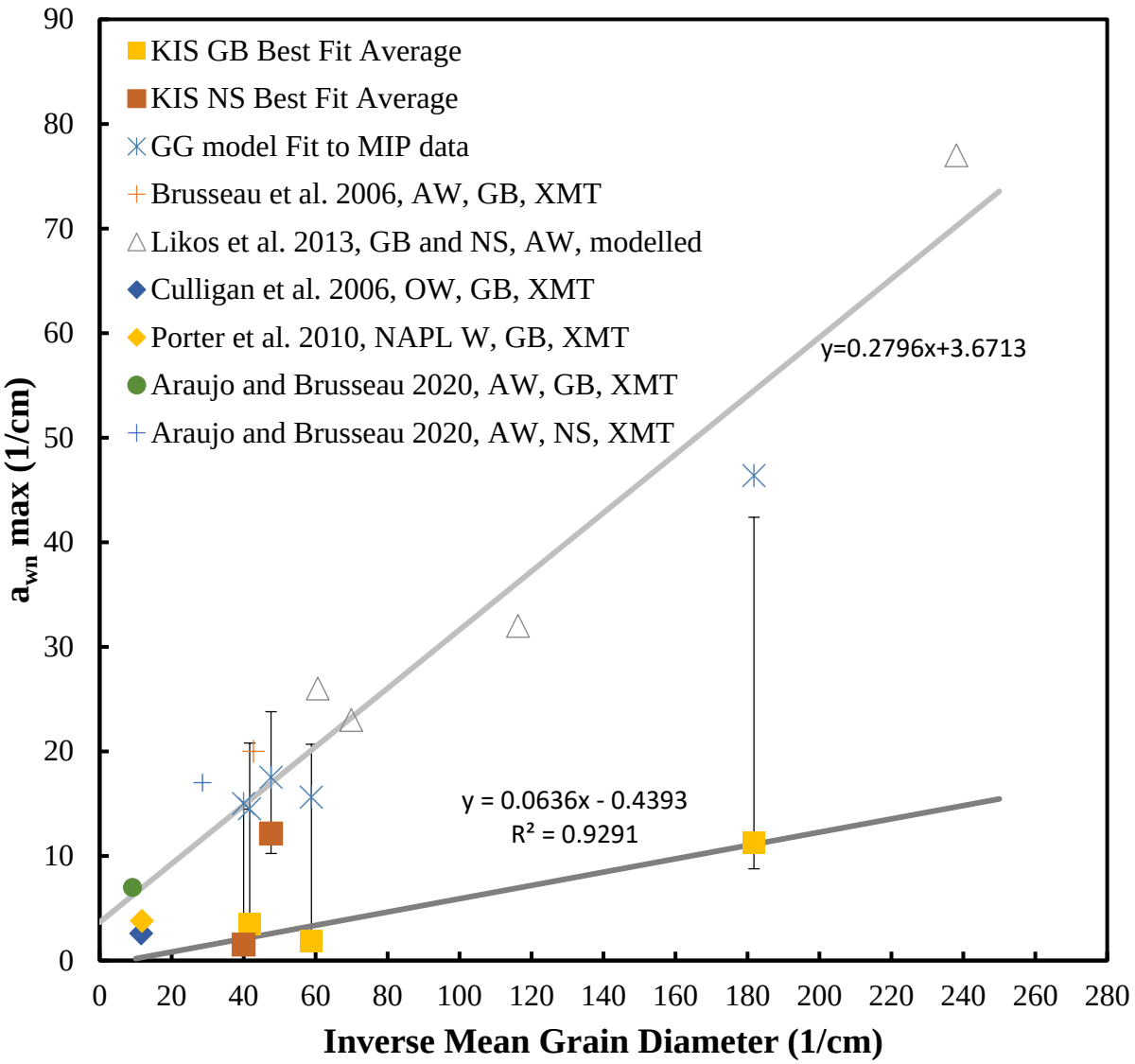

Figure 11: Mobile a_{wn}^{max} determined by KIS tracer experiment in an n-octane-water fluid system and comparison with literature data for capillary associated interfacial area.

4.3.3 Comparison of total specific interfacial area with literature data

Direct evaluation of the influence of grain diameters, their surface area and their fluid-fluid interfaces is difficult to perform for the entire set of published data because of the different types of surface area information reported, and because reported experiments are conducted with different types of fluid-porous media systems, e.g. air-water, NAPL-water, organic-liquid -water, etc. With very few exceptions, the literature compiled data contain IFA measured under residual-saturation conditions, i.e. imbibition conditions. Note, the interfacial area obtained for imbibition conditions is smaller.

Specific fluid-fluid interfaces reported in Brusseau et al. (2009; 2010) for organic-liquid-water fluid systems and at further data from (Kim et al. 1997; Zhong et al. 2016; Araujo and Brusseau 2020) are plotted against the inverse mean grain diameter on a log-log scale (Figure 12). It is

apparent that the general trend for all interfacial areas, a_{wn}^{max}, the a_{wn}^{max} measured by the KIS tracers, a_n^{max}, and a_n^{max} calculated with the geometric-based smooth sphere approach (GSSA) can be expressed as linear functions increasing with IMGD. The calculated total specific solid surface areas with the (Rootare and Prenzlow 1967) model applied to the MIP data match closely the linear trend reported values from the literature. For the two natural sands the a_n^{max} values (NS SSSA-MIP) are higher than the corresponding GSSA.

It can be observed that the total maximum IFA, a_n^{max} predicted by the (Grant and Gerhard 2007) model corresponding to the best fitted $a_{wn} - S_w$ curves for the five porous media are smaller than the linear trend of a_n^{max} of porous media with surface roughness from literature (Brusseau et al. 2010), and also smaller than the porous media with no surface roughness, or calculated with the GSSA (Brusseau et al. 2010). On the log-log scale, the linear functions are approximately parallel to each other. A much steeper increase of the a_n^{max} with IMGD is observed for the category of natural soils.

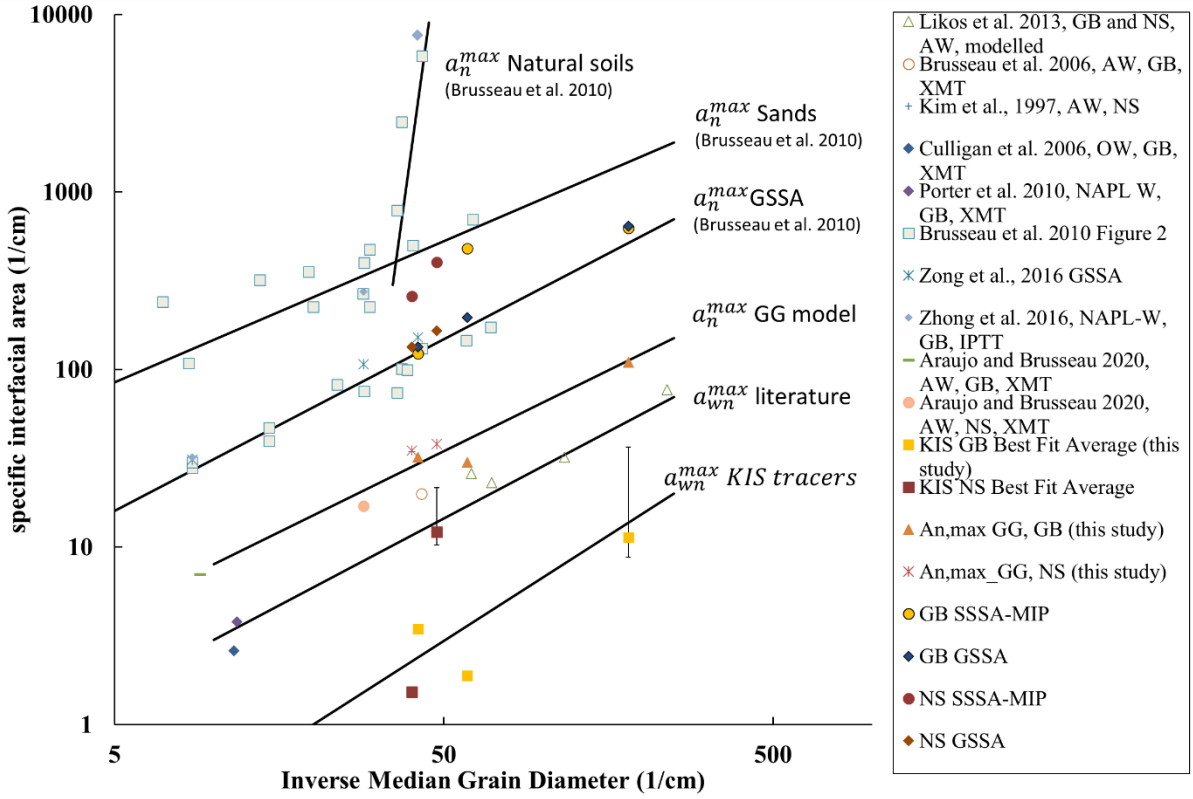

Figure 12: Compiled total specific IFA, a_n, and capillary-associated IFA, a_{wn}^{max} from the literature and this study. The total IFA for the five materials calculated as SSSA-MIP and GSSA, and the mobile capillary-associated IFAs determined with KIS tracer method

4.4 Texture influence on IFA

Here, we investigate the influence on a_{wn}^{max} of texture parameters: mean pore size, pore-uniformity coefficient, specific solid surface area, SSA geometrically calculated (GSSA), and grain roundness (Figure 13). A higher solid surface area, which incorporates a higher solid surface roughness, is correlated to a higher specific FIFA. For the five porous media, mean pore-sizes (measured with MIP) correlate well with the mean grain size (measured with DIA) (Figure

4). Therefore, when plotting a_{wn}^{max} with the mean pore size (Figure 13a) we see that the larger the mean pore-size the smaller the capillary-associated IFA.

The pore-size distribution is reflected in the pore-uniformity coefficient. Figure 13b) shows the influence on C_{pu} on a_{wn}^{max} . The specific solid-grain surface areas of the five materials were derived from the MIP measurements by applying the (Rootare and Prenzlow 1967) model, i.e., SSSA-MIP, and were also calculated geometrically using the smooth sphere assumption, i.e. GSSA. Their influence on the a_{wn}^{max} is plotted in Figure 13c) and d). In most literature studies the specific solid surface is measured with N_2/BET technique which commonly measures larger values than the SSSA-MIP and GSSA, e.g.(Narter and Brusseau 2010).

Generally, it can be concluded that the larger the SSSA the larger the a_{wn}^{max}. The very fine glass beads medium GB55 and the NS210 have the highest SSSA and the highest a_{wn}^{max} (**Table 1**). GB55 has the highest SSSA close to the GSSA value, 643 μm. GB55 resulting a_{wn}^{max}, is slightly smaller than the NS210 which has a large SSSA, measured by MIP. This is a further demonstration that the KIS tracer method can provide a robust characterization technique of fluid-fluid IFA, determine correctly the mobile capillary-associated IFA, since the same trend as in the literature is found. Similar to the findings of (Brusseau et al. 2009) for total FIFA, other texture parameters such as the grain- and pore-size distributions, roundness, Feret diameter, have minimal impact on the mobile capillary-associated IFA.

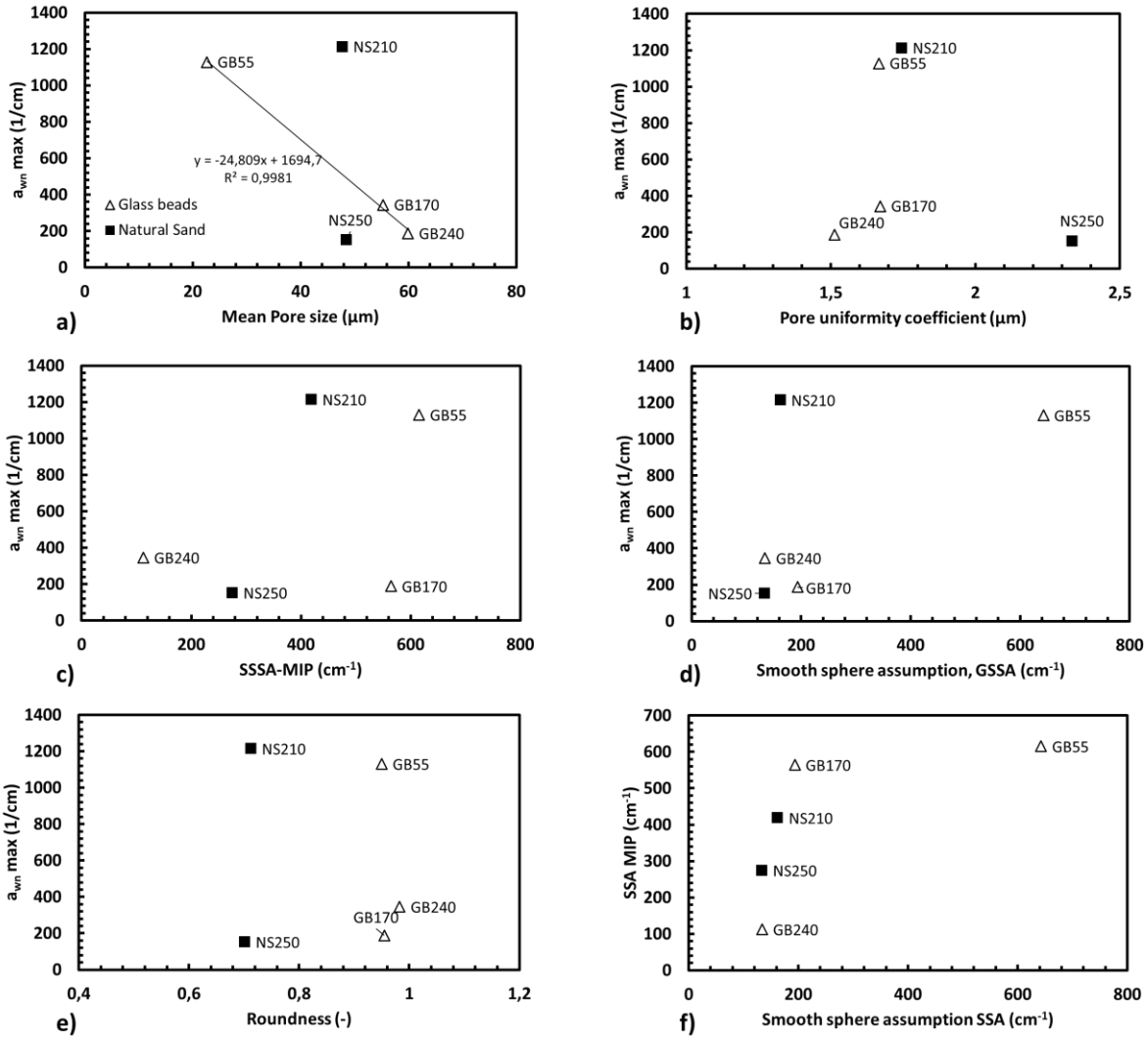

Figure 13: Specific capillary-associated IFA variation depending on the texture related parameters.

5 Conclusions

- We demonstrated that the KIS tracers allow studying the moving fluid-fluid interfaces in complex three-dimensional systems. On the basis of 15 sets of measurements performed on five different porous media, we were able to test and successfully extend the range of applicability of the KIS tracers, previously applied only to one type of glass-beads material. We were able to determine the specific capillary associated IFA and its linear relationship with the IMGD. We also observed new phenomena in the tracer BTC, not predicted by Darcy-scale coupled multiphase flow and reactive-transport models.
- The KIS tracer method can serve as a technique to improve our predictive capability of existing numerical schemes in constraining inverse models. The experimental results constitute an important data-set regarding the fate of an interface-depending reactive contaminant. The discrepancy between the experimental results and the numerical approaches underlines the limitation of existing approaches to fully resolve the processes taking place in the pore space. By

using the quantitative results obtained by the experiments, a future perspective is to attempt to match those by means of tuning average properties, like tortuosity, coordination number, while keeping in mind the processes affected by the pore geometry itself, e.g., non-Fickian transport.

- KIS tracer measured maximum specific FIFA magnitude increases linearly with inverse mean grain diameter, following a similar trend like the one reported in the literature (Costanza-Robinson and Brusseau 2002; Brusseau et al. 2009; Brusseau et al. 2010) obtained with other methods, e.g., IPTT and XMT. However, the values measured with the KIS tracer method range between 3.00 and 4.64 times smaller than the maximum capillary-associated IFA including both mobile and immobile parts, and, as expected, smaller than the total FIFA, a_n^{max}. The explanation for this observation is that the concentration of the reacted KIS tracer at the outflow is composed only of the solute transported with the mobile part of the water. Some fraction of the reacted solute becomes trapped in stagnant flow regions and it is never measured (to these add up the terminal menisci, pendular ring/ wedge menisci).
- We provide a compilation of the literature reported data for the specific fluid-fluid interfaces. Comparison of the measured and interpreted data herein with literature data provides further insights into the characterization of the fluid-fluid /NAPL-water interfaces. Similar to the observations made for the total specific interfacial area, natural sands, with higher roughness lead to larger capillary-associated IFA than the smooth glass beads. Other than the solid surface area we cannot make any conclusive statement about the influence on capillary-associated IFA of the other texture related parameters, e.g. grain- and pore-size distribution, uniformity coefficients, roundness, etc.
- The current continuum-scale (Darcy-scale) numerical models for reactive transport in two-phase flow in porous media need to be reconsidered. Many of the experimental breakthrough curves exhibit an early concentration peak and are flattening or decreasing towards the end of the drainage process. Current multiphase-flow models with reactive transport are unable to reproduce these effects. Therefore, to improve the predictive modelling capacities a new theoretical modeling framework is required.
- The micro-scale mechanisms need to be investigated separately with pore-scale and pore-network modelling of the reactive-transport and multiphase-flow-coupled processes. A promising approach to interpret the KIS tracer BTCs uses a pore-scale reactive transport model developed by Gao et al. (2020).
- For the future, the measurement accuracy of the KIS tracer method should be improved by adding pressure sensors to acquire information regarding the pressure change during the experiment, precise control of the flow rates attainable with high-precision pumps, development of a continuous sampling method to remove the errors during sampling.
- In addition, further research is needed to extend the applicability of the method to a wider range of flow conditions and fluid-fluid-porous media systems, e.g., natural soils, soils with wider variety of diameters and textures.

Until now the KIS tracer method has not been compared against another measurement technique. KIS tracers have the potential to be applied as a complementary technique for measuring FIFA. In this way, the mobile and the immobile parts of the capillary-associated IFA can be identified, or one can differentiate between mobile and immobile flow regions. This study represents an important step towards establishing KIS tracers as a robust characterization technique capable of measuring fluid-fluid interfacial area in multiphase flow in porous media systems.

Acknowledgments

This project was funded by the German Research Foundation, DFG, under project number 428614366, the European Community's 7th Framework Programme FP7 under grant number 309067 (trust-co2.org), and Horizon 2020 Research and Innovation Programme, FracRisk project (https://ec.europa.eu/inea/en/horizon-2020/projects/H2020-Energy/Shale-gas/FracRisk) under grant number 636811. We are grateful for the support of SFB1313 Collaborative Research Center (Project Number 327154368). We are also grateful to Florian Duschl and Dejian Zhou for the support with the laboratory work.

6 References

Annable MD, Rao PSC, Hatfield K, Graham WD, Wood AL, Enfield CG (1998) Partitioning Tracers for Measuring Residual NAPL: Field-Scale Test Results. J Environ Eng 124:498–503 . https://doi.org/10.1061/(ASCE)0733-9372(1998)124:6(498)

Anwar AHMF, Bettahar M, Matsubayashi U (2000) A method for determining air–water interfacial area in variably saturated porous media. J Contam Hydrol 43:129–146 . https://doi.org/10.1016/S0169-7722(99)00103-5

Araujo JB, Brusseau ML (2020) Assessing XMT-Measurement Variability of Air-Water Interfacial Areas in Natural Porous Media. Water Resour Res 56:e2019WR025470 . https://doi.org/10.1029/2019WR025470

Bradford SA, Leij FJ (1997) Estimating interfacial areas for multi-fluid soil systems. J Contam Hydrol 27:83–105 . https://doi.org/10.1016/S0169-7722(96)00048-4

Brooks RH, Corey AT (1964) Hydraulic properties of porous media. Hydrol Pap No 3 3:

Brusseau ML (2018) Assessing the potential contributions of additional retention processes to PFAS retardation in the subsurface. Sci Total Environ 613–614:176–185 . https://doi.org/10.1016/j.scitotenv.2017.09.065

Brusseau ML (2019) The influence of molecular structure on the adsorption of PFAS to fluid-fluid interfaces: Using QSPR to predict interfacial adsorption coefficients. Water Res 152:148–158 . https://doi.org/10.1016/j.watres.2018.12.057

Brusseau ML, Janousek H, Murao A, Schnaar G (2008) Synchrotron X-ray microtomography and interfacial partitioning tracer test measurements of NAPL-water interfacial areas. Water Resour Res 44:W01411 . https://doi.org/10.1029/2006WR005517

Brusseau ML, Narter M, Janousek H (2010) Interfacial partitioning tracer test measurements of organic-liquid/water interfacial areas: application to soils and the influence of surface roughness. Environ Sci Technol 44:7596–7600 . https://doi.org/10.1021/es101312n

Brusseau ML, Narter M, Schnaar G, Marble J (2009) Measurement and Estimation of Organic-Liquid/Water Interfacial Areas for Several Natural Porous Media. Environ Sci Technol 43:3619–3625 . https://doi.org/10.1021/es8020827

Brusseau ML, Ouni AE, Araujo JB, Zhong H (2015) Novel methods for measuring air–water interfacial area in unsaturated porous media. Chemosphere 127:208–213 . https://doi.org/10.1016/j.chemosphere.2015.01.029

Brusseau ML, Peng S, Schnaar G, Costanza-Robinson MS (2006) Relationships among air-water interfacial area, capillary pressure, and water saturation for a sandy porous medium. Water Resour Res 42:W03501 . https://doi.org/10.1029/2005WR004058

Brusseau ML, Peng S, Schnaar G, Murao A (2007) Measuring Air−Water Interfacial Areas with X-ray Microtomography and Interfacial Partitioning Tracer Tests. Environ Sci Technol 41:1956–1961 . https://doi.org/10.1021/es061474m

Cary JW (1994) Estimating the surface area of fluid phase interfaces in porous media. J Contam Hydrol 15:243–248 . https://doi.org/10.1016/0169-7722(94)90029-9

Cho J, Annable MD (2005) Characterization of pore scale NAPL morphology in homogeneous sands as a function of grain size and NAPL dissolution. Chemosphere 61:899–908 . https://doi.org/10.1016/j.chemosphere.2005.04.042

Costanza MS, Brusseau ML (2000) Contaminant Vapor Adsorption at the Gas−Water Interface in Soils. Environ Sci Technol 34:1–11 . https://doi.org/10.1021/es9904585

Costanza-Robinson MS, Brusseau ML (2002) Air-water interfacial areas in unsaturated soils: Evaluation of interfacial domains. Water Resour Res 38:1195 . https://doi.org/10.1029/2001WR000738

Culligan KA, Wildenschild D, Christensen BSB, Gray WG, Rivers ML (2006) Pore-scale characteristics of multiphase flow in porous media: A comparison of air–water and oil–water experiments. Adv Water Resour 29:227–238 . https://doi.org/10.1016/j.advwatres.2005.03.021

Dalla E, Hilpert M, Miller CT (2002) Computation of the interfacial area for two-fluid porous medium systems. J Contam Hydrol 56:25–48

Dobson R, Schroth MH, Oostrom M, Zeyer J (2006) Determination of NAPL−Water Interfacial Areas in Well-Characterized Porous Media. Environ Sci Technol 40:815–822 . https://doi.org/10.1021/es050037p

Flemisch B, Darcis M, Erbertseder K, Faigle B, Lauser A, Mosthaf K, Müthing S, Nuske P, Tatomir A, Wolff M, Helmig R (2011) DuMux: DUNE for multi-{phase, component, scale, physics, …} flow and transport in porous media. Adv Water Resour 34:1102–1112 . https://doi.org/10.1016/j.advwatres.2011.03.007

Fukunishi Y, Tateishi T, Suzuki M (1996) Octane/Water Interfacial Tension Calculation by Molecular Dynamics Simulation. J Colloid Interface Sci 180:188–192 . https://doi.org/10.1006/jcis.1996.0288

Gao H, Tatomir AB, Karadimitriou NK, Steeb H, Sauter M (2020) A two-phase, pore-scale reactive transport model for the kinetic interface- sensitive tracer (to be submitted). Water Resour Res

Grant GP, Gerhard JI (2007) Simulating the dissolution of a complex dense nonaqueous phase liquid source zone: 1. Model to predict interfacial area. Water Resour Res 43:W12410 . https://doi.org/10.1029/2007WR006038

Gvirtzman H, Roberts PV (1991) Pore scale spatial analysis of two immiscible fluids in porous media. Water Resour Res 27:1165–1176 . https://doi.org/10.1029/91WR00303

Hassanizadeh SM, Gray WG (1993) Thermodynamic basis of capillary pressure in porous media. Water Resour Res 29:3389–3405 . https://doi.org/10.1029/93WR01495

Hassanizadeh SM, Gray WG (1990) Mechanics and thermodynamics of multiphase flow in porous media including interphase boundaries. Adv Water Resour 13:169–186 . https://doi.org/10.1016/0309-1708(90)90040-B

Heiß VI, Neuweiler I, Ochs S, Färber A (2011) Experimental investigation on front morphology for two-phase flow in heterogeneous porous media. Water Resour Res 47:W10528 . https://doi.org/10.1029/2011WR010612

Held RJ, Celia MA (2001) Pore-scale modeling extension of constitutive relationships in the range of residual saturations. Water Resour Res 37:165–170 . https://doi.org/10.1029/2000WR900234

Hilfer R, Øren PE (1996) Dimensional analysis of pore scale and field scale immiscible displacement. Transp Porous Media 22:53–72 . https://doi.org/10.1007/BF00974311

Jiang H, Guo B, Brusseau ML (2020) Pore-Scale Modeling of Fluid-Fluid Interfacial Area in Variably Saturated Porous Media Containing Microscale Surface Roughness. Water Resour Res 56:e2019WR025876 . https://doi.org/10.1029/2019WR025876

Joekar-Niasar V, Hassanizadeh SM (2012a) Analysis of Fundamentals of Two-Phase Flow in Porous Media Using Dynamic Pore-Network Models: A Review. Crit Rev Environ Sci Technol 42:1895–1976 . https://doi.org/10.1080/10643389.2011.574101

Joekar-Niasar V, Hassanizadeh SM (2012b) Uniqueness of Specific Interfacial Area–Capillary Pressure–Saturation Relationship Under Non-Equilibrium Conditions in Two-Phase Porous Media Flow. Transp Porous Media 94:465–486 . https://doi.org/10.1007/s11242-012-9958-3

Karadimitriou NK, Joekar-Niasar V, Babaei M, Shore CA (2016) Critical Role of the Immobile Zone in Non-Fickian Two-Phase Transport: A New Paradigm. Environ Sci Technol 50:4384–4392 . https://doi.org/10.1021/acs.est.5b05947

Kim H, Rao PSC, Annable MD (1997) Determination of effective air-water interfacial area in partially saturated porous media using surfactant adsorption. Water Resour Res 33:2705 . https://doi.org/10.1029/97WR02227

Kim H, Rao PSC, Annable MD (1999) Gaseous Tracer Technique for Estimating Air–Water Interfacial Areas and Interface Mobility. Soil Sci Soc Am J 63:1554–1560 . https://doi.org/10.2136/sssaj1999.6361554x

Lenormand R, Touboul E, Zarcone C (1988) Numerical models and experiments on immiscible displacements in porous media. J Fluid Mech 189:165–187 . https://doi.org/10.1017/S0022112088000953

Leverett MC (1941) Capillary Behavior in Porous Solids. Trans AIME 142:152–169 . https://doi.org/10.2118/941152-G

Likos WJ, Jaafar R (2013) Pore-Scale Model for Water Retention and Fluid Partitioning of Partially Saturated Granular Soil. J Geotech Geoenvironmental Eng 139:724–737 . https://doi.org/10.1061/(ASCE)GT.1943-5606.0000811

929 Lyu Ying, Brusseau Mark L., El Ouni Asma, Araujo Juliana B., Su Xiaosi (2017) The Gas-
930 Absorption/Chemical-Reaction Method for Measuring Air-Water Interfacial Area in Natural
931 Porous Media. Water Resour Res 53:9519–9527 . https://doi.org/10.1002/2017WR021717

932 McDonald K, Carroll KC, Brusseau ML (2016) Comparison of fluid-fluid interfacial areas measured with X-
933 ray microtomography and interfacial partitioning tracer tests for the same samples. Water
934 Resour Res 52:5393–5399 . https://doi.org/10.1002/2016WR018775

935 Miller CT, Poirier-McNeil MM, Mayer AS (1990) Dissolution of Trapped Nonaqueous Phase Liquids: Mass
936 Transfer Characteristics. Water Resour Res 26:2783–2796 .
937 https://doi.org/10.1029/WR026i011p02783

938 Narter M, Brusseau ML (2010) Comparison of Interfacial partitioning tracer test and high-resolution
939 microtomography measurements of fluid-fluid interfacial areas for an ideal porous medium.
940 Water Resour Res 46: . https://doi.org/10.1029/2009WR008375

941 Nelson NT, Brusseau ML (1996) Field Study of the Partitioning Tracer Method for Detection of Dense
942 Nonaqueous Phase Liquid in a Trichloroethene- Contaminated Aquifer. Environ Sci Technol
943 30:2859–2863 . https://doi.org/10.1021/es960148b

944 Niemi A, Bensabat J, Shtivelman V, Edlman K, Gouze P, Luguot L, Hingl F, Benson SM, Pezard P,
945 Rasmusson K, Tian L, Fagerlund F, Tatomir AB, Lange, Torsten, Sauter M, Freifeld B (2016)
946 Overview of the Heletz site, its characterization and data analysis for CO2 injection and
947 geological storage (submitted). Int J Greenh Gas Control xx:

948 Oostrom M, White MD, Brusseau ML (2001) Theoretical estimation of free and entrapped nonwetting–
949 wetting fluid interfacial areas in porous media. Adv Water Resour 24:887–898 .
950 https://doi.org/10.1016/S0309-1708(01)00017-3

951 Patmonoaji A, Tsuji K, Muharrik M, Suekane T (2018) Micro-tomographic analyses of specific interfacial
952 area inside unconsolidated porous media with differing particle characteristics from microscopic
953 to macroscopic scale. J Colloid Interface Sci 532:614–621 .
954 https://doi.org/10.1016/j.jcis.2018.08.023

955 Peche A, Halisch M, Bogdan Tatomir A, Sauter M (2016) Development of a numerical workflow based on
956 µ-CT imaging for the determination of capillary pressure–saturation-specific interfacial area
957 relationship in 2-phase flow pore-scale porous-media systems: a case study on Heletz sandstone.
958 Solid Earth 7:727–739 . https://doi.org/10.5194/se-7-727-2016

959 Peng S, Brusseau ML (2005) Impact of soil texture on air-water interfacial areas in unsaturated sandy
960 porous media. Water Resour Res 41: . https://doi.org/10.1029/2004WR003233

961 Porter ML, Wildenschild D, Grant G, Gerhard JI (2010) Measurement and prediction of the relationship
962 between capillary pressure, saturation, and interfacial area in a NAPL-water-glass bead system.
963 Water Resour Res 46:W08512 . https://doi.org/10.1029/2009WR007786

964 Reeves PC, Celia MA (1996) A Functional Relationship Between Capillary Pressure, Saturation, and
965 Interfacial Area as Revealed by a Pore-Scale Network Model. Water Resour Res 32:2345 .
966 https://doi.org/10.1029/96WR01105

967 Rootare HM, Prenzlow CF (1967) Surface areas from mercury porosimeter measurements. J Phys Chem
968 71:2733–2736 . https://doi.org/10.1021/j100867a057

969 Saripalli KP, Kim H, Rao PSC, Annable MD (1997) Measurement of Specific Fluid−Fluid Interfacial Areas of
970 Immiscible Fluids in Porous Media. Environ Sci Technol 31:932–936 .
971 https://doi.org/10.1021/es960652g

972 Schaefer CE, DiCarlo DA, Blunt MJ (2000) Determination of Water-Oil Interfacial Area during 3-Phase
973 Gravity Drainage in Porous Media. J Colloid Interface Sci 221:308–312 .
974 https://doi.org/10.1006/jcis.1999.6604

975 Schaffer M, Maier F, Licha T, Sauter M (2013) A new generation of tracers for the characterization of
976 interfacial areas during supercritical carbon dioxide injections into deep saline aquifers: Kinetic
977 interface-sensitive tracers (KIS tracer). Int J Greenh Gas Control 14:200–208 .
978 https://doi.org/10.1016/j.ijggc.2013.01.020

979 Schnaar G, Brusseau ML (2006) Characterizing Pore-Scale Configuration of Organic Immiscible Liquid in
980 Multiphase Systems With Synchrotron X-Ray Microtomography. Vadose Zone J 5:641–648 .
981 https://doi.org/10.2136/vzj2005.0063

982 Simon MA, Brusseau ML (2007) Analysis of a gas-phase partitioning tracer test conducted in an
983 unsaturated fractured-clay formation. J Contam Hydrol 90:146–158 .
984 https://doi.org/10.1016/j.jconhyd.2006.09.010

985 Tatomir A, Maier F, Schaffer M, Licha T, Sauter M (2013) Modelling of Kinetic Interface Sensitive Tracers
986 for Two-Phase Systems. In: Hou MZ, Xie H, Were P (eds) Clean Energy Systems in the Subsurface:
987 Production, Storage and Conversion. Springer Berlin Heidelberg, pp 65–74

988 Tatomir A, Vriendt KD, Zhou D, Gao H, Duschl F, Sun F, Licha T, Sauter M (2018) Kinetic Interface
989 Sensitive Tracers: Experimental Validation in a Two-Phase Flow Column Experiment. A Proof of
990 Concept. Water Resour Res 54:10,223-10,241 . https://doi.org/10.1029/2018WR022621

991 Tatomir AB, Halisch M, Duschl F, Peche A, Wiegand B, Schaffer M, Licha T, Niemi A, Bensabat J, Sauter M
992 (2016a) An integrated core-based analysis for the characterization of flow, transport and
993 mineralogical parameters of the Heletz pilot CO2 storage site reservoir. Int J Greenh Gas Control
994 48, Part 1:24–43 . https://doi.org/10.1016/j.ijggc.2016.01.030

995 Tatomir AB, Jyoti A, Sauter M (2016b) The Monitoring of CO2 plume migration in deep saline formations
996 with kinetic interface sensitive tracers. In: Singh TN, Vikram V (eds) Geologic Carbon
997 Sequestration: Understanding Reservoir Concepts. Springer, p 336

998 Tatomir AB, Schaffer M, Kissinger A, Hommel J, Nuske P, Licha T, Helmig R, Sauter M (2015) Novel
999 approach for modeling kinetic interface-sensitive (KIS) tracers with respect to time-dependent
1000 interfacial area change for the optimization of supercritical carbon dioxide injection into deep
1001 saline aquifers. Int J Greenh Gas Control 33:145–153 .
1002 https://doi.org/10.1016/j.ijggc.2014.11.020

1003 Washburn EW (1921) Note on a Method of Determining the Distribution of Pore Sizes in a Porous
1004 Material. Proc Natl Acad Sci U S A 7:115–116

Zhong H, El Ouni A, Lin D, Wang B, Brusseau ML (2016) The two-phase flow IPTT method for measurement of nonwetting-wetting liquid interfacial areas at higher nonwetting saturations in natural porous media. Water Resour Res 52:5506–5515 . https://doi.org/10.1002/2016WR018783

7 Appendix

Table SI 1. Best fitting parameters for the modelling of the KIS tracer experiments: 1) calibration of the volume ratio of the n-octane and water; 2) calibration of the 2-NSA concentration BTC.

Experiment index	Volume ratio V_n/V_T BTC							2-NSA Concentration BTC			S_w at end of experiment	
	Q_{min} (ml/min)	Q_{max} (ml/min)	Q_{BF} (ml/min)	K_{min} (m^2)	K_{max} (m^2)	K_{BF} (m^2)	RMSE	a_0	a_{wn}^{max} (m^{-1})	RMSE	Experiment	Model
GB55_1	0.6	0.64	0.61	2×10^{-13}	6×10^{-13}	6×10^{-13}	0.045241	1×10^{-5}	848	0.3162	0.18	0.36
GB55_3	0.54	0.58	0.55	1×10^{-13}	5×10^{-13}	5×10^{-13}	0.009795	1.5×10^{-5}	1270	1.2831	0.16	0.37
GB55_4	0.56	0.60	0.57	4×10^{-13}	8×10^{-13}	8×10^{-13}	0.026996	1.5×10^{-5}	1270	0.8899	0.2	0.37
GB170_2	0.53	0.57	0.55	8×10^{-13}	12×10^{-13}	1.1×10^{-12}	0.05649	5×10^{-6}	141	0.5561	0.26	0.35
GB170_3	0.67	0.71	0.68	5.8×10^{-12}	6.2×10^{-12}	6×10^{-12}	0.052176	5×10^{-6}	141	0.5145	0.27	0.36
GB170_6	0.62	0.66	0.62	3.0×10^{-12}	7.0×10^{-12}	5×10^{-12}	0.0129	1×10^{-5}	282	1.5397	0.28	0.35
GB240_1	0.42	0.46	0.44	1.0×10^{-12}	5.0×10^{-12}	2×10^{-12}	0.018418	2×10^{-5}	519	2.3039	0.27	0.36
GB240_2	0.65	0.68	0.65	4.0×10^{-12}	6.0×10^{-12}	4×10^{-12}	0.018708	1×10^{-5}	260	1.839	0.35	0.35
GB240_3	0.66	0.70	0.66	1.0×10^{-12}	5.0×10^{-12}	4×10^{-12}	0.023005	1×10^{-5}	260	1.5397	0.31	0.36
NS210_3	0.60	0.64	0.62	5.0×10^{-13}	9.0×10^{-13}	8×10^{-13}	0.0289	4×10^{-5}	1120	1.0787	0.35	0.38
NS210_4	0.62	0.66	0.65	7.0×10^{-13}	11×10^{-13}	8×10^{-13}	0.01687	3×10^{-5}	841	0.8517	0.38	0.37
NS210_5	0.61	0.65	0.64	4.0×10^{-13}	8.0×10^{-13}	6×10^{-13}	0.023323	6×10^{-5}	1680	0.5484	0.32	0.37
NS250_1	0.70	0.74	0.73	5.0×10^{-12}	9.0×10^{-12}	5×10^{-12}	0.0133	1×10^{-5}	241	1.3005	0.44	0.39
NS250_2	0.76	0.80	0.76	5.0×10^{-12}	9.0×10^{-12}	9×10^{-12}	0.015451	5×10^{-5}	121	1.6447	0.43	0.43
NS250_3	0.46	0.50	0.46	1.0×10^{-12}	5.0×10^{-12}	3×10^{-12}	0.017759	4×10^{-5}	96.5	0.9524	0.48	0.43

To calculate the capillary number for the Darcy-scale column experiments we apply the following transformation (Hilfer and Øren 1996):

$$Ca = \frac{\mu_i v_D L}{p_d K}$$

where μ_i is the dynamic viscosity of the invading fluid, $v_D$is the mean Darcy velocity of the invading fluid, $p_d$is the entry pressure of the nonwetting fluid into the porous material, and K is the intrinsic permeability.

Table SI 2. Calculated capillary number, *Ca*

Experiment	K $(\boldsymbol{m^2})$	φ (-)	$\boldsymbol{p_d}$ $(\boldsymbol{Pa})$	$\boldsymbol{v_D}$ $(\boldsymbol{m/s})$	Ca
GB55_1	6E-13	0.411	5937	3.5E-05	**1.228**
GB55_3	5.00E-13	0.411	5937	3.16E-05	**1.329**
GB55_4	8.00E-13	0.411	5937	3.27E-05	**0.861**
GB170_2	1.10E-12	0.455	1819	2.85E-05	**1.781**
GB170_3	6.00E-12	0.455	1819	3.52E-05	**0.404**
GB170_6	5.00E-12	0.455	1819	3.21E-05	**0.442**
GB240_1	2.00E-12	0.464	1606	2.24E-05	**0.870**
GB240_2	4.00E-12	0.464	1606	3.3E-05	**0.643**
GB240_3	4.00E-12	0.464	1606	3.35E-05	**0.653**
NS210_3	8.00E-13	0.432	2050	3.38E-05	**2.579**
NS210_4	8.00E-13	0.432	2050	3.55E-05	**2.704**
NS210_5	6.00E-13	0.432	2050	3.49E-05	**3.55**
NS250_1	5.00E-12	0.445	1642	3.87E-05	**0.589**
NS250_2	9.00E-12	0.445	1642	4.03E-05	**0.341**
NS250_3	3.00E-12	0.445	1642	2.44E-05	**0.618**

Table SI 3. Data sets used for the total specific interfacial areas (after Brusseau et al. 2010)

Porous medium	S_n	No. measurements	Data Source
Vinton Soil	0.15	4	(Brusseau et al. 2010)
Eustis soil	0.17	4	(Brusseau et al. 2010)
Mixed sand	0.26	2	(Brusseau et al. 2008)
45-50 mesh sand	0.17	8	(Brusseau et al. 2008)
12-20 mesh sand	0.29	6	(Dobson et al. 2006)
20-30 mesh sand	0.28	5	(Dobson et al. 2006)
30-40 mesh sand	0.27	6	(Dobson et al. 2006)
40-50 mesh sand	0.28	5	(Dobson et al. 2006)
10-12 mesh sand	0.12	1	(Cho and Annable 2005)
20-30 mesh sand	0.14	1	(Cho and Annable 2005)
30-40 mesh sand	0.12	1	(Cho and Annable 2005)
40-60 mesh sand	0.15	1	(Cho and Annable 2005)
80-100 mesh sand	0.16	1	(Cho and Annable 2005)
40-100 mesh sand	0.19	3	(Saripalli et al. 1997)
40-50 mesh sand	Variable	5	(Schaefer et al. 2000)

S_n- saturation of organic liquid

1027